

## Low-energy moiré phonons in twisted bilayer van der Waals heterostructures

Jonathan Z. Lu<sup>1,\*</sup> Ziyan Zhu<sup>1,†</sup> Mattia Angeli<sup>1,2</sup> Daniel T. Larson<sup>1</sup> and Efthimios Kaxiras<sup>1,2</sup><sup>1</sup>Department of Physics, Harvard University, Cambridge, Massachusetts 02138, USA<sup>2</sup>John A. Paulson School of Engineering and Applied Sciences, Harvard University, Cambridge, Massachusetts 02138, USA

(Received 12 July 2022; revised 15 September 2022; accepted 23 September 2022; published 10 October 2022)

We develop a low-energy continuum model for phonons in twisted moiré bilayers, based on a configuration space approach. In this approach, interatomic force constants are obtained from density functional theory (DFT) calculations of *untwisted* bilayers with various in-plane shifts. This allows for efficient computation of phonon properties for any small twist angle, while maintaining DFT-level accuracy. Based on this framework, we show how the low-energy phonon modes, including interlayer shearing and layer breathing modes, vary with the twist angle. As the twist angle decreases, the frequencies of the low-energy modes are reordered and the atomic displacement fields corresponding to phonon eigenmodes break translational symmetry, developing periodicity on the moiré length scale. We demonstrate the capabilities of our model by calculating the phonon properties of three specific structures: Bilayer graphene, bilayer molybdenum disulfide ( $\text{MoS}_2$ ), and molybdenum diselenide-tungsten diselenide ( $\text{MoSe}_2\text{-WSe}_2$ ).

DOI: [10.1103/PhysRevB.106.144305](https://doi.org/10.1103/PhysRevB.106.144305)

## I. INTRODUCTION

Two-dimensional (2D) van der Waals (vdW) multilayer structures can be constructed by stacking 2D materials in a layer-by-layer fashion. If the stacking involves a twist of one layer by an angle  $\theta$  with respect to the next layer, the relative misorientation between atomic lattices produces a moiré interference pattern with a length scale larger than the lattice constants of the individual layers. Such moiré bilayers can give rise to localized electronic states and tunable electronic properties [1–7]. In twisted bilayer graphene, superconductivity and other unconventional correlated states have been observed when the twist angle  $\theta$  takes values near the “magic angle” [8–11]. Similar behavior has been shown in twisted bilayers composed of transition metal dichalcogenides (TMDCs), albeit often with decreased sensitivity to the twist angle [12–24]. Determination of the role of phonons is a crucial step toward an understanding of these strongly correlated electronic states, particularly superconductivity [25–28]. The collective vibration of a twisted bilayer can be strongly affected by the moiré pattern, forming the so-called moiré phonons [28,29]. Moiré phonons are also of general experimental interest, and have recently been observed in graphene [30]. The variation of phonon properties with the twist angle allows Raman spectroscopy to be used to help characterize moiré bilayers [31–35].

The interplay of two distinct length scales and the large number of atoms within a moiré cell make calculations of the phonon properties extremely challenging. Due to the rapid

scaling in computational cost with respect to the moiré length, direct calculations of phonons using density functional theory (DFT) are currently not feasible for twist angles less than a few degrees. Moreover, DFT calculations using periodic supercells can only be carried out for a specific set of commensurate angles. Instead, a continuum approximation has been successfully used to model the electronic structure and atomic relaxation of twisted bilayers and trilayers [36–42]. Continuum models have also been considered for moiré phonon analysis. The most efficient of these are empirical continuum models, but they leave out important details such as the out-of-plane degree of freedom and phonon modes that require coupling, for instance the shearing and layer breathing modes [29].

We propose a first-principles-based continuum model of moiré phonons, similar to the one developed by Quan *et al.* [35] to help interpret the Raman spectra of twisted  $\text{MoS}_2$  bilayers, but we have extended it to momenta beyond the  $\Gamma$  point and have applied the model to several different bilayer systems. To bypass the need to compute the interatomic forces for all atoms in a large moiré supercell, we adopt a configuration space formalism to describe the local atomic environment. This approach has been used as the basis for a continuum model of atomic relaxations in twisted vdW heterostructures [41,43–46]. Using this model we obtain the low-energy phonon properties of bilayer graphene, bilayer  $\text{MoS}_2$ , and a  $\text{MoSe}_2\text{-WSe}_2$  heterostructure, and show how a relative twist between the layers modifies the phonon frequencies and eigenmodes.

The paper is organized as follows. In Sec. II we derive the moiré dynamical matrix in configuration space, including twist-angle-dependent relaxation [41]. We then compare our model predictions to the results of three other approaches in Sec. III. In Sec. IV we apply our model to three representative moiré bilayers and analyze their band structure and real space

\*jlu@college.harvard.edu

†Present address: Stanford Institute for Materials and Energy Sciences, SLAC National Accelerator Laboratory, Menlo Park, CA 94025, USA; ziyanzhu@stanford.edu

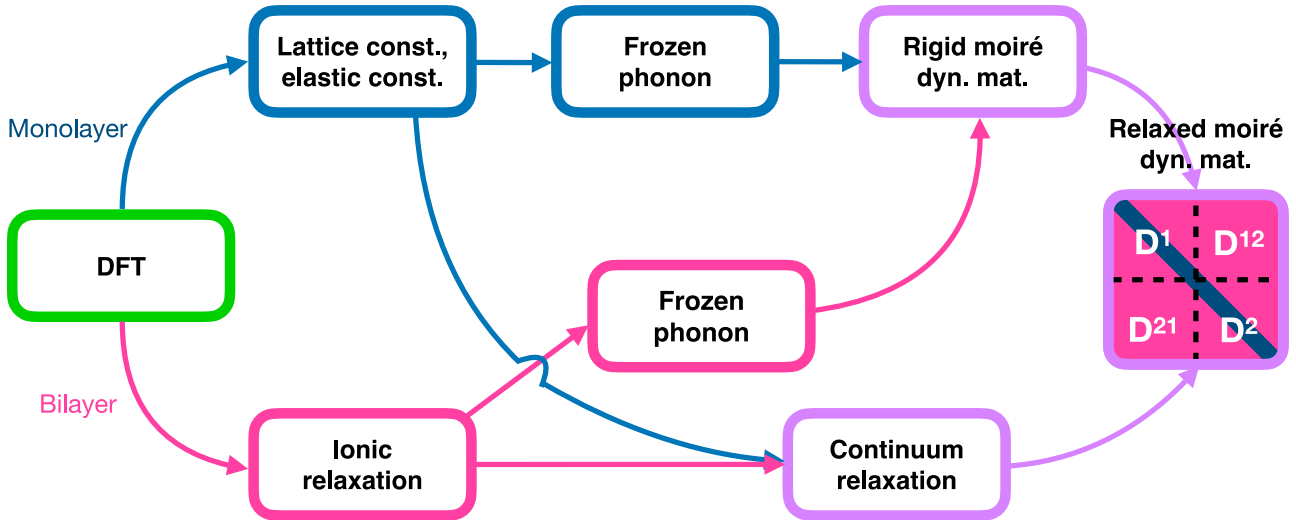


FIG. 1. Schematic representation of the numerical implementation of the CSC model. A collection of monolayer (blue) and bilayer (pink) calculations are combined into a rigid (unrelaxed) moiré dynamical matrix and used to determine the bilayer relaxation pattern (both purple). All of these elements are combined to form the relaxed moiré dynamical matrix. The square labeled “relaxed moiré dynamical matrix” formally represents the dynamical matrix construction: The diagonal blocks are from the monolayer calculations whereas the off-diagonal blocks are constructed from the stacking dependent force field calculations.

atomic displacements. Finally, we summarize our results and their implications in Sec. V.

## II. CONFIGURATION SPACE CONTINUUM MODEL

The workflow of our configuration space continuum (CSC) model is summarized in Fig. 1. We first construct the moiré dynamical matrix by computation of the dynamical matrices of many rigidly shifted bilayers—one for each configuration of atoms in layer 1 with respect to layer 2—and the individual monolayers. From the monolayer we obtain the optimized lattice constant and the elastic constants that are used for relaxation. We relax the ionic positions of each shifted bilayer as well, keeping the horizontal positions of one atom per layer fixed to maintain the registry between the layers. We then compute atomic forces using the frozen phonon approach, which under the CSC formalism produces the unrelaxed (rigid) moiré dynamical matrix. Finally, we include twist-dependent relaxation which yields the relaxed moiré form of the dynamical matrix. We provide a derivation of the model in this section, and details of the calculations can be found in Appendices A and B. Throughout the derivation, we use tildes to indicate a quantity in the moiré supercell, and when referring to the dynamical matrix we use a bar to denote the matrix in real space (the absence of the bar means the matrix is expressed in Fourier space).

### A. Moiré dynamical matrix

The phonon spectrum of a crystal can be obtained by diagonalizing the dynamical matrix with the basis expanded in momentum space. The moiré dynamical matrix at a point  $\tilde{\mathbf{k}}$  in the moiré Brillouin zone, which we call the center site, is represented generically as a layer-block matrix encoding intralayer (diagonal) and interlayer (off-diagonal)

couplings:

$$D_{\text{moiré}}(\tilde{\mathbf{k}}) = \begin{bmatrix} D^1(\tilde{\mathbf{k}}) & D^{12} \\ D^{12*} & D^2(\tilde{\mathbf{k}}) \end{bmatrix}. \quad (1)$$

Each block of the moiré dynamical matrix depends on two reciprocal space degrees of freedom,  $\mathbf{k}^{(\ell)}$  and  $\mathbf{k}^{(\ell')}$ , which are momenta from the monolayer Brillouin zones of layers  $\ell$  and  $\ell'$ . This is because in a twisted system, the interatomic forces depend not only on the pairwise distance of two atoms, but also the position of the atom due to the change of the local environment.

### B. Moiré scattering selection rule

We first derive how the degrees of freedom in the basis of Eq. (1) are connected to each other through a selection rule. We begin with a monolayer, which is the intralayer term that has no stacking dependence. Considering only one layer  $\ell$ , the monolayer phonon equation of motion can be expressed as

$$\sum_{j\nu\beta} \bar{D}_{\mu\nu\alpha\beta}^{\ell}(\mathbf{R}_i - \mathbf{R}_j) \delta\hat{u}_{j\ell\nu\beta} = \omega^2 \delta\hat{u}_{i\ell\mu\alpha}, \quad (2)$$

where  $\bar{D}_{\mu\nu\alpha\beta}^{\ell}(\mathbf{R}_i - \mathbf{R}_j)$  is the dynamical matrix element,  $\mathbf{R}_i$  is a monolayer lattice vector,  $\mu, \nu$  are Cartesian degrees of freedom,  $\alpha, \beta$  are sublattice degrees of freedom, and  $\delta\hat{u}_{i\ell\mu\alpha}$  is the phonon displacement component that corresponds to atom  $\alpha$  in direction  $\mu$ . We can define a phonon displacement in the Bloch basis as follows,

$$\delta\hat{u}_{i\ell\mu\alpha}(\mathbf{k}^{(\ell)}) = \frac{1}{\sqrt{|\Gamma^*|}} e^{i\mathbf{k}^{(\ell)} \cdot \mathbf{R}_i} \delta u_{\ell\mu\alpha}(\mathbf{k}^{(\ell)}), \quad (3)$$

where  $\mathbf{k}^{(\ell)}$  is a momentum degree of freedom in  $\Gamma^{(\ell)*}$ , the monolayer Brillouin zone of layer  $\ell$  with area  $|\Gamma^*|$ . We first note the orthogonality relation

$$\sum_{\mu\alpha} \delta\hat{u}_{i\ell\mu\alpha}^* \delta\hat{u}_{j\ell\mu\alpha} = \delta_{ij}. \quad (4)$$

To expand the equation of motion, Eq. (2), in the Fourier basis, we multiply both sides by  $\delta\hat{u}_{k\ell\mu\alpha}^*$ , then sum over  $k$ ,  $\mu$ ,

and  $\alpha$ :

$$\sum_{jk\mu\nu\alpha\beta} \bar{D}_{\mu\nu\alpha\beta}^{\ell}(\mathbf{R}_i - \mathbf{R}_j) \delta\hat{u}_{k\ell\mu\alpha}^* \delta\hat{u}_{j\ell\nu\beta} = \omega^2 \sum_{k\mu\alpha} \delta\hat{u}_{k\ell\mu\alpha}^* \delta\hat{u}_{i\ell\mu\alpha}. \quad (5)$$

Using Eq. (4),

$$\sum_{ij\mu\nu\alpha\beta} \bar{D}_{\mu\nu\alpha\beta}^{\ell}(\mathbf{R}_i - \mathbf{R}_j) \delta\hat{u}_{i\ell\mu\alpha}^* \delta\hat{u}_{j\ell\nu\beta} = \omega^2. \quad (6)$$

Relabeling  $\mathbf{R} = \mathbf{R}_i$ ,  $\Delta\mathbf{R} = \mathbf{R}_i - \mathbf{R}_j$  and changing to the Bloch basis using Eq. (3) yields

$$\frac{1}{|\Gamma^*|} \sum_{\mathbf{R}} \left[ e^{-i(\mathbf{k}^{(\ell)} - \mathbf{k}'^{(\ell)}) \cdot \mathbf{R}} \sum_{\mu\nu\alpha\beta} \bar{D}_{\mu\nu\alpha\beta}(\Delta\mathbf{R}) e^{-i\mathbf{k}'^{(\ell)} \cdot \Delta\mathbf{R}} \delta u_{\ell\mu\alpha}^*(\mathbf{k}^{(\ell)}) \delta u_{\ell\nu\beta}(\mathbf{k}'^{(\ell)}) \right] = \omega^2. \quad (7)$$

Note the Poisson resummation rule:

$$\sum_{\mathbf{R}} e^{-i(\mathbf{k}^{(\ell)} - \mathbf{k}'^{(\ell)}) \cdot \mathbf{R}} = |\Gamma^*| \sum_{\mathbf{G}^{(\ell)}} \delta(\mathbf{k}^{(\ell)} - \mathbf{k}'^{(\ell)} - \mathbf{G}^{(\ell)}), \quad (8)$$

where  $\mathbf{G}^{(\ell)}$  is a reciprocal lattice vector in layer  $\ell$ . Defining  $D_{\mu\nu\alpha\beta}(\mathbf{k}'^{(\ell)})$  as

$$D_{\mu\nu\alpha\beta}(\mathbf{k}'^{(\ell)}) = \sum_{\Delta\mathbf{R}} \bar{D}_{\mu\nu\alpha\beta}(\Delta\mathbf{R}) e^{-i\mathbf{k}'^{(\ell)} \cdot \Delta\mathbf{R}}, \quad (9)$$

the phonon equation of motion becomes

$$\sum_{\mu\nu\alpha\beta} D_{\mu\nu\alpha\beta}(\mathbf{k}^{(\ell)}) \delta u_{\ell\mu\alpha}^*(\mathbf{k}^{(\ell)}) \delta u_{\ell\nu\beta}(\mathbf{k}^{(\ell)}) = \omega^2, \quad (10)$$

for each  $\mathbf{G}^{(\ell)}$ , since the phonon displacement  $\delta u_{i\ell\mu\alpha}$  is the same at  $\mathbf{k}^{(\ell)}$  and  $\mathbf{k}^{(\ell)} + \mathbf{G}^{(\ell)}$ . Equation (10) is equivalent to

$$\mathbf{D}(\mathbf{k}^{(\ell)}) \cdot \delta \mathbf{u}(\mathbf{k}^{(\ell)}) = \omega^2 \delta \mathbf{u}(\mathbf{k}^{(\ell)}), \quad (11)$$

which is the eigenvalue equation that describes the intralayer phonon at  $\mathbf{k}^{(\ell)}$ , and the dynamical matrix  $D(\mathbf{k}^{(\ell)})$  can be computed using either density functional perturbation theory or frozen phonon approaches.

In a moiré cell the dynamical matrix gains an additional degree of freedom because the forces depend not only on the difference in lattice vectors, but also the real space position itself due to the twist. The general phonon equation of motion is given as the following:

$$\sum_{j\nu\beta\ell'} \bar{D}_{\mu\nu\alpha\beta}(\mathbf{R}_i, \mathbf{R}_j) \delta\hat{u}_{j\ell'\nu\beta} = \omega^2 \delta\hat{u}_{i\ell\mu\alpha}, \quad (12)$$

where  $\mathbf{R}_i$  and  $\mathbf{R}_j$  correspond to the atomic positions on layers  $\ell$  and  $\ell'$ , respectively. Similarly to the intralayer term, we multiply both sides of the equation by  $\delta\hat{u}_{i\ell\mu\alpha}^*$  and sum over  $\mu$ ,  $\alpha$ , and  $\ell$ . Plugging in the definition in Eq. (3),

$$\sum_{\mu\nu\alpha\beta\ell\ell'} D_{\tilde{\mathbf{k}}\mu\nu\alpha\beta}(\mathbf{k}^{(\ell)}, \mathbf{k}^{(\ell')}) \delta u_{\ell\mu\alpha}^*(\mathbf{K}^{(\ell)}) \delta u_{\ell'\nu\beta}(\mathbf{K}^{(\ell')}) = \omega^2, \quad (13)$$

where

$$D_{\tilde{\mathbf{k}}\mu\nu\alpha\beta}(\mathbf{k}^{(\ell)}, \mathbf{k}^{(\ell')}) = \frac{1}{|\Gamma^*|} \sum_{ij} \bar{D}_{\mu\nu\alpha\beta}(\mathbf{R}_i, \mathbf{R}_j) e^{-i\mathbf{K}^{(\ell)} \cdot \mathbf{R}_i} e^{i\mathbf{K}^{(\ell')} \cdot \mathbf{R}_j}, \quad (14)$$

and  $\mathbf{K}^{(\ell)} = \tilde{\mathbf{k}} + \mathbf{k}^{(\ell)}$  is an expansion for small momentum  $\mathbf{k}^{(\ell)}$  about a given point  $\tilde{\mathbf{k}}$  in the moiré Brillouin zone. Making a two-center approximation such that  $\bar{D}_{\mu\nu\alpha\beta}(\mathbf{R}_i, \mathbf{R}_j) = \bar{D}_{\mu\nu\alpha\beta}(\mathbf{R}_i - \mathbf{R}_j)$ , we can then perform a Fourier expansion on  $\bar{D}_{\mu\nu\alpha\beta}(\mathbf{R}_i - \mathbf{R}_j)$ :

$$\bar{D}_{\mu\nu\alpha\beta}(\mathbf{R}_i - \mathbf{R}_j) = \int \frac{d^2\mathbf{p}}{(2\pi)^2} e^{i\mathbf{p} \cdot (\mathbf{R}_i - \mathbf{R}_j)} D_{\mu\nu\alpha\beta}(\mathbf{p}). \quad (15)$$

Note that despite the two-center approximation, the momentum space dynamical matrix  $D_{\tilde{\mathbf{k}}\mu\nu\alpha\beta}$  still depends on two different momenta from the opposite layers  $\ell$  and  $\ell'$ . Using Eq. (15) as well as Eq. (8) in Eq. (14) yields

$$\begin{aligned} D_{\tilde{\mathbf{k}}\mu\nu\alpha\beta}(\mathbf{k}^{(\ell)}, \mathbf{k}^{(\ell')}) &= \frac{1}{|\Gamma^*|} \int \frac{d^2\mathbf{p}}{(2\pi)^2} D_{\mu\nu\alpha\beta}(\mathbf{p}) \sum_{ij} e^{-i(\mathbf{K}^{(\ell)} + \mathbf{p}) \cdot \mathbf{R}_i} e^{i(\mathbf{K}^{(\ell')} + \mathbf{p}) \cdot \mathbf{R}_j} \\ &= \frac{|\Gamma^*|}{(2\pi)^2} \sum_{\mathbf{G}^{(\ell)} \mathbf{G}^{(\ell')}} \int d^2\mathbf{p} D_{\mu\nu\alpha\beta}(\mathbf{p}) \delta(\mathbf{K}^{(\ell)} + \mathbf{p} - \mathbf{G}^{(\ell)}) \delta(\mathbf{K}^{(\ell')} + \mathbf{p} - \mathbf{G}^{(\ell')}) \end{aligned}$$

$$= \frac{1}{|\Gamma|} \sum_{\mathbf{G}^{(\ell)} \mathbf{G}^{(\ell')}} D_{\mu\nu\alpha\beta}(\tilde{\mathbf{k}} + \mathbf{k}^{(\ell)} - \mathbf{G}^{(\ell)}) \delta_{\mathbf{k}^{(\ell')} - \mathbf{k}^{(\ell)}, \mathbf{G}^{(\ell')} - \mathbf{G}^{(\ell)}}, \quad (16)$$

where  $|\Gamma|$  is the area of the monolayer unit cell and we note that  $|\Gamma| = (2\pi)^2/|\Gamma^*|$ . The  $\delta$  function imposes a selection rule that constrains the allowed values of  $\mathbf{k}^{(\ell)}$  and  $\mathbf{k}^{(\ell')}$ . For concreteness, we define each reciprocal lattice vector as

$$\mathbf{G}_{mn}^{(\ell)} = m\mathbf{g}_1^{(\ell)} + n\mathbf{g}_2^{(\ell)}, \quad (17)$$

where  $\mathbf{g}_1^{(\ell)}$  and  $\mathbf{g}_2^{(\ell)}$  are a reciprocal lattice basis for layer  $\ell$ . Neglecting higher-order coupling, we assume that only terms with equal  $m, n$  in  $\mathbf{G}^{(\ell)}$  and  $\mathbf{G}^{(\ell')}$  are nonzero, so the above simplifies to

$$D_{\tilde{\mathbf{k}}\mu\nu\alpha\beta}(\mathbf{k}^{(\ell)}, \mathbf{k}^{(\ell')}) = \frac{1}{|\Gamma|} \sum_{mn} D_{\mu\nu\alpha\beta}(\tilde{\mathbf{k}} + \mathbf{k}^{(\ell)} - \mathbf{G}_{mn}^{(\ell)}) \delta_{\mathbf{k}^{(\ell)} - \mathbf{k}^{(\ell')}, \tilde{\mathbf{G}}_{mn}}. \quad (18)$$

The difference  $\mathbf{G}_{mn}^{(\ell)} - \mathbf{G}_{mn}^{(\ell')}$  between corresponding reciprocal lattice vectors from each layer is a moiré reciprocal lattice vector  $\tilde{\mathbf{G}}_{mn}$ . Without loss of generality, taking  $\ell = 1$  and  $\ell' = 2$ , Eq. (18) imposes a constraint on the momenta given by

$$\mathbf{k}^{(1)} - \mathbf{k}^{(2)} = \mathbf{G}_{mn}^{(2)} - \mathbf{G}_{mn}^{(1)} = -\tilde{\mathbf{G}}_{mn}. \quad (19)$$

We henceforth drop the subscripts on  $\tilde{\mathbf{G}}$  for clarity. Equation (18) is the fundamental equation governing the moiré dynamical matrix. The stacking-dependent part of the moiré phonon equation of motion becomes

$$\begin{aligned} \frac{1}{|\Gamma|} \sum_{\nu\beta\ell'} \sum_{\tilde{\mathbf{G}}} D_{\mu\nu\alpha\beta}(\tilde{\mathbf{k}} + \mathbf{k}^{(\ell)} - \mathbf{G}^{(\ell)}) \delta u_{\ell'\nu\beta}(\mathbf{K}^{(\ell')} - \tilde{\mathbf{G}}) \\ = \omega^2 \delta u_{\ell\mu\alpha}(\mathbf{K}^{(\ell)}), \end{aligned} \quad (20)$$

where we note that  $\tilde{\mathbf{G}}$  and  $\mathbf{G}^{(\ell)}$  are in one-to-one correspondence via Eq. (19). To simplify the above we choose a gauge  $\mathbf{k}^{(\ell)} = \mathbf{G}^{(\ell)}$  (though other gauges will work, and we will choose a different one to justify the construction of the moiré dynamical matrix) with  $\ell \neq \ell'$ . Without loss of generality, we let  $\ell = 1$ :

$$\begin{aligned} D_{\mu\nu\alpha\beta}(\tilde{\mathbf{k}} + \mathbf{k}^{(1)} - \mathbf{G}^{(1)}) &= D_{\mu\nu\alpha\beta}(\mathbf{k} + \mathbf{G}^{(2)} - \mathbf{G}^{(1)}) \\ &= D_{\mu\nu\alpha\beta}(\tilde{\mathbf{k}} - \tilde{\mathbf{G}}). \end{aligned} \quad (21)$$

Note that reciprocal space has sufficient symmetry that any choice of a pair of signs for  $\mathbf{k}$  and  $\tilde{\mathbf{G}}$  produces the same term above.

Combining the monolayer term [Eq. (11)] and the twist-dependent term [Eq. (20)], we obtain the moiré dynamical matrix. We verified numerically that the magnitude of the dynamical matrix decays rapidly with distance from the  $\Gamma$  point, so it suffices to expand up to the first shell of the moiré reciprocal lattice, which contains six vectors  $\tilde{\mathbf{G}}_1, \dots, \tilde{\mathbf{G}}_6$ . For the off-diagonal terms, we ignore the  $\tilde{\mathbf{k}}$  dependence. The interlayer term is explicitly given as follows:

$$D^{12} = \begin{bmatrix} D_{\mu\nu\alpha\beta}^{12}(\tilde{\mathbf{G}}_0) & D_{\mu\nu\alpha\beta}^{12}(\tilde{\mathbf{G}}_1) & \dots & D_{\mu\nu\alpha\beta}^{12}(\tilde{\mathbf{G}}_6) \\ D_{\mu\nu\alpha\beta}^{12}(-\tilde{\mathbf{G}}_1) & D_{\mu\nu\alpha\beta}^{12}(\tilde{\mathbf{G}}_0) & & \\ \vdots & & \ddots & \\ D_{\mu\nu\alpha\beta}^{12}(-\tilde{\mathbf{G}}_6) & & & D_{\mu\nu\alpha\beta}^{12}(\tilde{\mathbf{G}}_0) \end{bmatrix}, \quad (22)$$

where  $D_{\mu\nu\alpha\beta}^{ij}(\tilde{\mathbf{G}})$  is a submatrix of the dynamical matrix at  $\tilde{\mathbf{G}}$  with rows (columns) corresponding to degrees of freedom due to layer  $i$  ( $j$ ). The  $(i, j)$  block thus represents phonon hoppings between reciprocal lattice sites  $\tilde{\mathbf{G}}_i$  and  $\tilde{\mathbf{G}}_j$ . We have disregarded a small number of first-shell terms above that do not live along the first row, first column, or the diagonal, after having verified that their inclusion negligibly affects the numerical results. That is, we ignore hoppings that do not include  $\tilde{\mathbf{G}}_0$ . Similarly for the intralayer term,

$$D^i(\tilde{\mathbf{k}}) = \begin{bmatrix} D_P^i(\tilde{\mathbf{k}} + \tilde{\mathbf{G}}_0) & D_{\mu\nu\alpha\beta}^{ii}(\tilde{\mathbf{G}}_1) & \dots & D_{\mu\nu\alpha\beta}^{ii}(\tilde{\mathbf{G}}_6) \\ D_{\mu\nu\alpha\beta}^{ii}(-\tilde{\mathbf{G}}_1) & D_P^i(\tilde{\mathbf{k}} + \tilde{\mathbf{G}}_1) & & \\ \vdots & & \ddots & \\ D_{\mu\nu\alpha\beta}^{ii}(-\tilde{\mathbf{G}}_6) & & & D_P^i(\tilde{\mathbf{k}} + \tilde{\mathbf{G}}_6) \end{bmatrix}, \quad (23)$$

where the diagonal terms are the dynamical matrix of the pristine monolayer  $D_P^i(\tilde{\mathbf{k}} + \tilde{\mathbf{G}})$  and the off-diagonal terms are the twist-dependent intralayer term constructed from Eq. (20) when  $\ell = \ell'$ .

### C. Dynamical matrix in configuration space

We are particularly interested in structures with a small twist angle, which means the moiré cell contains a large number of primitive cells and consequently many atoms. In order to make the model computationally feasible, we express  $D_{\mu\nu\alpha\beta}$  in terms of a collection of local atomic environments, known as configuration space [41]. Within the continuum approximation we replace the primitive cell lattice vectors  $\mathbf{R}$  with a continuous variable  $\mathbf{r}$  defined throughout the moiré cell, and allow quantities of interest to be defined at all  $\mathbf{r}$ . At each location  $\mathbf{r}$  the local environment can be approximated by an untwisted bilayer with a horizontal shift of one layer relative to the other. We specify the interlayer shift by  $\mathbf{b}(\mathbf{r})$ , and the space formed by all  $\mathbf{b}$  is configuration space. It is in one-to-one correspondence with real space by a linear transformation

$$\mathbf{b}(\mathbf{r}) = (\mathbb{1} - A_2 A_1^{-1}) \mathbf{r}, \quad (24)$$

where  $A_i$  is a matrix whose columns are the primitive lattice vectors of layer  $i$  and  $\mathbb{1}$  is the  $2 \times 2$  identity matrix. This correspondence also gives a useful relationship between the reciprocal lattice vectors of the moiré cell,  $\tilde{\mathbf{G}}$ , and those of the

primitive unit cell,  $\mathbf{G}$ :

$$\tilde{\mathbf{G}} \cdot \mathbf{r} = \mathbf{G} \cdot \mathbf{b}(\mathbf{r}). \quad (25)$$

Using these concepts, we can express the momentum space dynamical matrix as follows:

$$\begin{aligned} D_{\mu\nu\alpha\beta}^{\text{rig}}(\tilde{\mathbf{k}} + \tilde{\mathbf{G}}) &= \frac{1}{\sqrt{|\Gamma^*|}} \int d^2\mathbf{r} \bar{D}_{\mu\nu\alpha\beta}(\mathbf{r}) e^{i(\tilde{\mathbf{k}} + \tilde{\mathbf{G}}) \cdot \mathbf{r}} \\ &= \frac{1}{\sqrt{|\Gamma^*|}} \int d^2\mathbf{b} \bar{D}_{\mu\nu\alpha\beta}(\mathbf{b}) e^{i(\mathbf{k} + \mathbf{G}) \cdot \mathbf{b}} \\ &\approx \frac{1}{\sqrt{|\Gamma^*|} N^2} \sum_{\mathbf{b} \in \mathcal{S}(N)} \bar{D}_{\mu\nu\alpha\beta}^{(\mathbf{b})} e^{i(\mathbf{k} + \mathbf{G}) \cdot \mathbf{b}}. \end{aligned} \quad (26)$$

The factor of  $|\Gamma|$ , arising from discretization, cancels out the normalization from Eq. (18). Configuration space allows us to replace  $\bar{D}(\mathbf{r})$ , which we cannot easily determine, with  $\bar{D}(\mathbf{b})$ , which we can readily compute with DFT for a primitive bilayer cell with any specified shift  $\mathbf{b}$ . In the small  $\theta$  limit the local environment varies slowly and smoothly with  $\mathbf{b}$ , so we can approximate the integral over  $\mathbf{b}$  with the sum over a  $N \times N$  uniform mesh  $\mathcal{S}(N)$  of  $\mathbf{b}$  values. Since  $\mathcal{S}(N)$  is uniform,  $D_{\mu\nu\alpha\beta}^{\text{rig}}(\tilde{\mathbf{k}} + \tilde{\mathbf{G}})$  describes a moiré bilayer with a uniform distribution of local configurations. In other words, it represents a rigid moiré structure with no twist-induced continuum relaxation, which is a good approximation for  $\theta$  sufficiently large. We describe the procedure for including relaxation effects in the next subsection.

#### D. Continuum relaxation

We emphasize that in all structures considered here atomic relaxation to the lowest-energy (equilibrium) configuration is included. However, its effect varies as a function of twist angle: For moderate to small twist angles, twist-induced atomic relaxation is much more important than for large twist angles. The range of angles over which the atomic relaxation is important varies by material, but relaxation typically begins to have a significant impact for twist angles smaller than about  $2^\circ$ . In real space, atomic relaxation results in enlarged areas of the lowest-energy stacking configurations (AB and BA in graphene) at the expense of high-energy stackings (AA), with domain walls forming in between. In configuration space relaxation can be viewed as a higher density of configurations in the lowest-energy stackings [41,42]. This can be accounted for by shifting each  $\mathbf{b}$  in the uniform mesh  $\mathcal{S}(N)$  by an angle-dependent relaxation displacement vector  $\mathbf{u}_\theta(\mathbf{b})$ , yielding a nonuniform mesh  $\mathbf{B} = \mathbf{b} + \mathbf{u}_\theta(\mathbf{b})$  denoted  $\mathcal{S}_\theta(N)$ . We use linear elasticity theory to describe the intralayer energy, combined with the generalized stacking fault energy (GSFE) functional for the interlayer energy. (The GSFE parameters are given in Appendix A.) By minimizing the total energy we can compute  $\mathbf{u}_\theta(\mathbf{b})$  in configuration space. We refer to Carr *et al.* [41] and Zhu *et al.* [42] for a detailed overview of continuum relaxation. The dynamical matrix can then be updated by Fourier interpolation, using an inverse transform

$$\bar{D}_{\mu\nu\alpha\beta}^{(\mathbf{B})}(\tilde{\mathbf{k}}) = \frac{1}{\sqrt{|\Gamma^*|}} \sum_{\tilde{\mathbf{G}}} D_{\mu\nu\alpha\beta}^{\text{rig}}(\tilde{\mathbf{k}} + \tilde{\mathbf{G}}) e^{-i(\mathbf{k} + \mathbf{G}) \cdot \mathbf{B}}, \quad (27)$$

followed by a second forward transform, which arrives at the following relaxed moiré dynamical matrix:

$$D_{\mu\nu\alpha\beta}(\tilde{\mathbf{k}} + \tilde{\mathbf{G}}) = \frac{1}{\sqrt{|\Gamma^*|} N^2} \sum_{\mathbf{b} \in \mathcal{S}(N)} \bar{D}_{\mu\nu\alpha\beta}^{(\mathbf{B})}(\tilde{\mathbf{k}}) e^{i(\mathbf{k} + \mathbf{G}) \cdot \mathbf{b}}. \quad (28)$$

To obtain the real space phonon vibration pattern, we perform an inverse Fourier transform by summing over components of the eigenvectors as follows,

$$\delta u_{n\ell\mu\alpha\tilde{\mathbf{G}}}(\mathbf{r}) = \sum_{\tilde{\mathbf{G}}} \delta u_{n\ell\mu\alpha\tilde{\mathbf{G}}}(\tilde{\mathbf{k}}) e^{i(\tilde{\mathbf{G}} + \tilde{\mathbf{k}}) \cdot \mathbf{r}}, \quad (29)$$

where  $n$  is the band index and  $\delta u_{n\ell\mu\alpha\tilde{\mathbf{G}}}$  is the eigenvector component that corresponds to  $\tilde{\mathbf{G}}$ .

#### E. Acoustic sum rules

Even though the total forces are fixed to be zero in the force field calculations of individual stackings, the combination of all configurations in the moiré dynamical matrix construction modifies the total force of the combined system. Therefore, an acoustic sum of the moiré dynamical matrix is required to ensure the total force stays zero in addition to the sum rules on the unrotated bilayers and monolayers. We use a correction matrix (chosen without loss of generality to be diagonal in the latter pair of indices)

$$C_{\mu\nu\alpha\alpha} = \sum_{\beta} \sqrt{\frac{M_{\beta}}{M_{\alpha}}} D_{\text{moiré},\mu\nu\beta\alpha}^*(\Gamma), \quad (30)$$

where  $D_{\text{moiré},\mu\nu\beta\alpha}^*(\Gamma)$  is the moiré dynamical matrix by replacing the pristine monolayer blocks  $D_P(\mathbf{k} + \tilde{\mathbf{G}})$  with  $D_P(\Gamma)$ , as we enforce translational invariance only at the  $\Gamma$  point and enforce continuity everywhere else. We then adjust  $D_{\text{moiré}}(\tilde{\mathbf{k}}) \leftarrow D_{\text{moiré}}(\tilde{\mathbf{k}}) - C$ , observing numerically that the above approximation satisfies adequately the translational invariance constraint. The sum rule is adapted from Quan *et al.* [35].

### III. MODEL VALIDATION

To validate our CSC model, we compare results obtained from it with two first-principles models, namely direct DFT on the moiré supercell for a small system where such calculations are feasible, and with molecular dynamics (MD) simulations that employ an interatomic potential [28,47]. We also compare our CSC results to another empirical continuum (EC) model adapted from Koshino and Son [29].

#### A. Comparison with molecular dynamics and DFT

Direct DFT phonon calculations on the moiré cell are the most accurate but are restricted by the size of the cell. MD simulations allow for larger supercell sizes, but have inherent limitations on accuracy due to the choice of interatomic potential. Both direct DFT and MD are computationally expensive and require a commensurate supercell. Since the CSC model uses DFT inputs in a well-defined approximation, it should reflect the direct DFT and MD calculations reasonably well and does not suffer constraints based on moiré supercell size or commensurability. We choose a twist angle,  $\theta = 7.34^\circ$ , that gives a commensurate pattern in bilayer graphene for these comparisons.

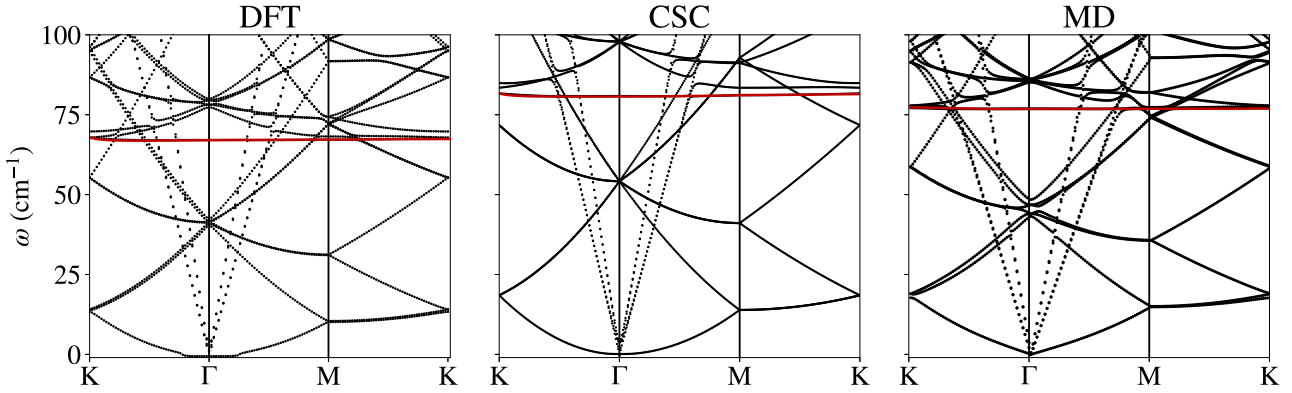


FIG. 2. Comparison of phonon band at  $\theta = 7.34^\circ$  between DFT (left panel), CSC (middle panel), and MD (right panel) calculations for graphene. The LB mode is highlighted in red.

Figure 2 compares the phonon bands of the CSC model, MD simulations, and direct DFT phonon calculations on the moiré supercell at  $\theta = 7.34^\circ$ . The layer breathing (LB) mode, which represents layer 1 (2) moving in the  $-z$  ( $+z$ ) direction and a much weaker in-plane motion, is highlighted in red in each case. The results from the three models are qualitatively quite similar, validating the CSC construction. The quantita-

tive differences, such as the exact frequency of the LB mode, are to be expected due to the specific choices made for each model, such as the exchange correlation functional for DFT and the interatomic potential for MD.

In addition to the phonon dispersion relations, Fig. 3 shows a comparison of the atomic displacements of the LB mode in graphene, corresponding to the red band in Fig. 2 at the

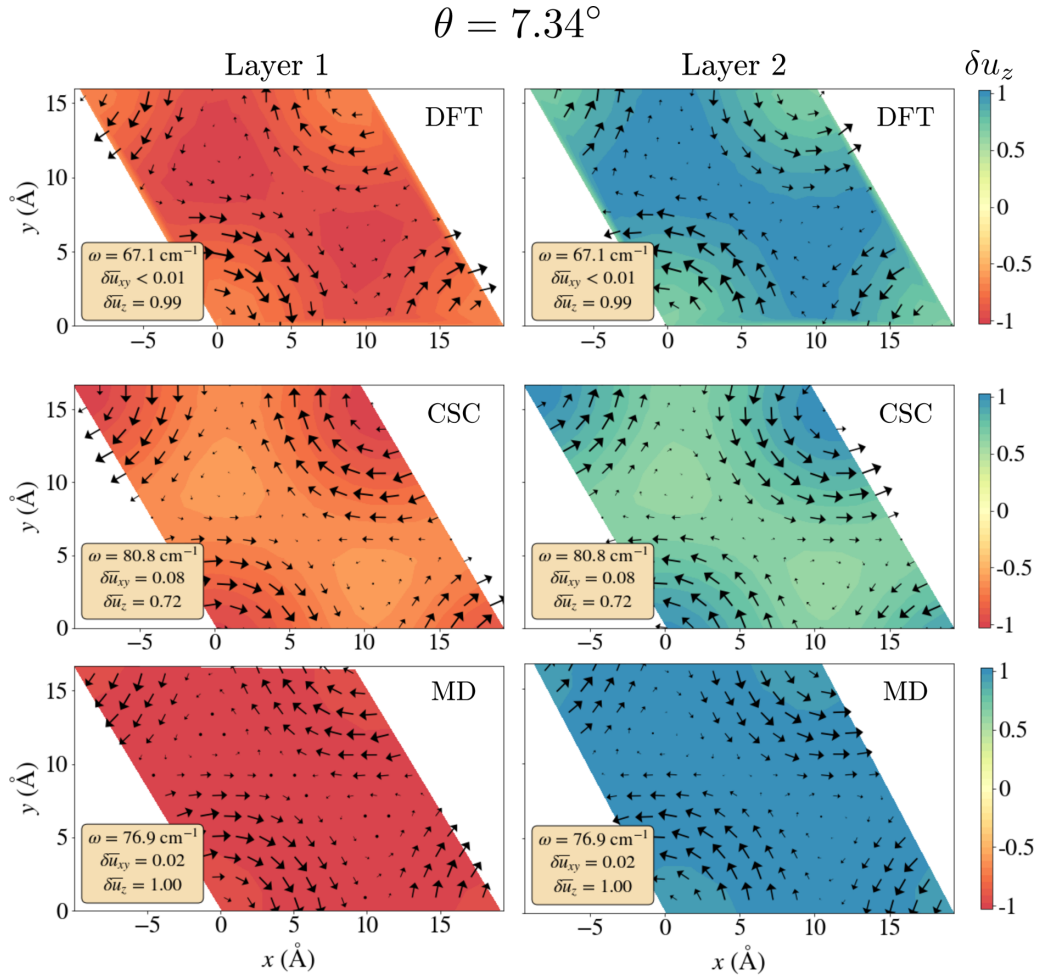


FIG. 3. Comparison of the LB atomic displacements between direct DFT, CSC, and MD. Each model has normalized its displacements  $\delta u$  separately, in arbitrary units. The insets show the frequency and average displacement magnitude in-plane ( $\delta u_{xy}$ ) and out-of-plane ( $\delta u_z$ ).

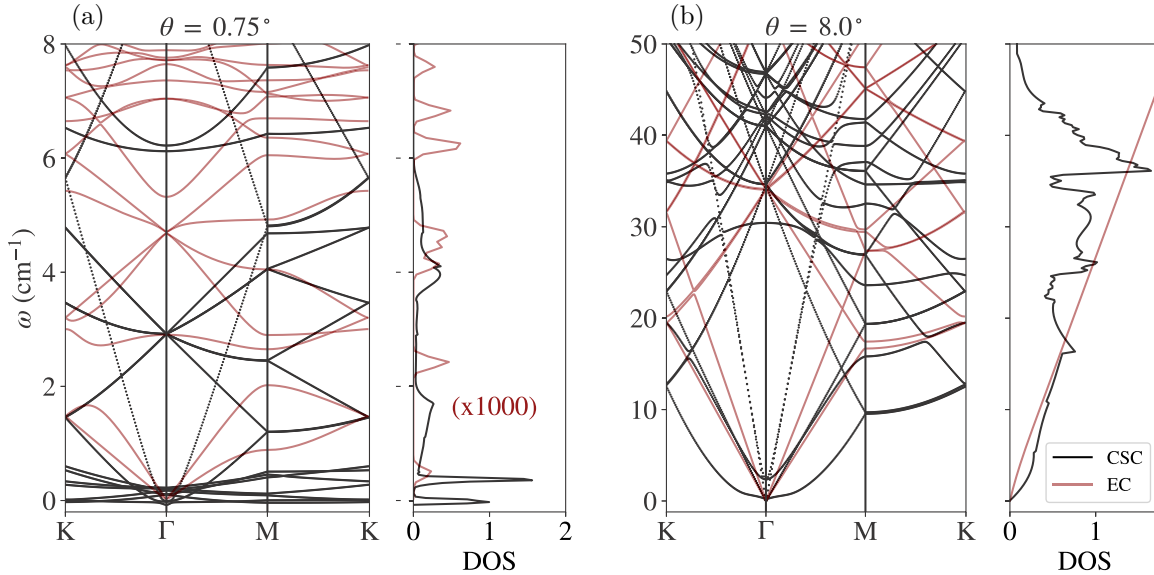


FIG. 4. Comparison of the phonon bands and DOS for bilayer MoS<sub>2</sub> at (a) 0.75° and (b) 8.0° as calculated using the EC model (red lines) and the CSC model (black lines). For  $\theta = 0.75^\circ$ , the EC DOS has been scaled by a factor of 1000 for visualization.

$\Gamma$  point. We focus on a qualitative comparison of the geometrical structure. All models exhibit a swirling in-plane motion around the AA regions at the corner of the moiré supercell. The primary difference between the models is the variation in the out-of-plane motion. In the DFT calculation the maximum vertical displacement occurs in the AB regions, whereas for the CSC model the maximum is in the AA regions. While the MD calculation shows some variation in the vertical displacement between AA and AB spots and the maximum vertical displacement also occurs in the AB regions as in DFT, it is mostly uniform throughout the moiré cell. The reason for the quantitative difference between the CSC and the first-principles models is likely due to the breakdown of the continuum approximation at a large angle. When the twist angle is large, as is the case for  $\theta = 7.34^\circ$  in graphene, the local stacking order varies drastically from one real space position to a neighboring one. However, the CSC still assumes a smooth variation of the force fields in real space, which causes the real space LB mode to be similar for all twist angles and thus it fails to capture the change in the large angle. Despite this slight disagreement, both the LB frequency and the band structure from the CSC show an excellent agreement with first-principles calculations (Fig. 3). Their agreement in the LB mode out-of-plane displacement field is better at smaller twist angles (not shown in Fig. 3); that is, all three models exhibit maxima in the displacement field around the AA regions.

### B. Comparison with empirical continuum model

The EC model, based on empirical interlayer interactions, is the most efficient of the models discussed in this section [29]. In Fig. 4 we compare the phonon dispersion relations and density of states for MoS<sub>2</sub>, obtained with the EC model and with our CSC model. To obtain the in-plane phonon modes, we perturb around the relaxed equilibrium positions by adding a kinetic energy contribution to the inter-

layer and intralayer terms of the dynamical matrix. We then solve the equation of motion to obtain the phonon modes. We use the GSFE coefficients and elastic constants provided in Tables I and II for the CSC model. A detailed derivation is given in Appendix C.

The EC model has a free empirical parameter that we determine by scaling the bands such that the lowest-frequency in-plane translational modes at  $K$  coincide in the two models; the scaling factor is 2.3 for  $\theta = 0.75^\circ$  and 22.5 for 8.0°.

There is little agreement between the two models for small  $\theta$ , as shown in Fig. 4(a). The EC model predicts flatter bands and exhibits a gap between 2 and 3 cm<sup>-1</sup>, whereas no such features occur in the CSC model. Moreover, the slopes of the in-plane acoustic modes cannot be matched well. Intrinsically, the EC model also does not include any out-of-plane motion, such as the  $z$ -translational mode, nor does it include interlayer modes such as the shearing (S) mode. The LB mode is absent in the EC model for these two reasons. Our continuum model does not suffer from such limitations.

In the large twist-angle limit, Fig. 4(b), the results from the two models agree for low frequencies near  $\Gamma$ ; they both exhibit linear DOS relations and the position of the first folded band cluster is near 35 cm<sup>-1</sup>.

TABLE I. GSFE coefficients of MoS<sub>2</sub>, graphene, and MoSe<sub>2</sub>-WSe<sub>2</sub> heterostructure. All in units of meV per unit cell.

	MoS <sub>2</sub>	Graphene	MoSe <sub>2</sub> -WSe <sub>2</sub>
$c_0$	25.91	6.985	27.07
$c_1$	12.79	4.111	13.31
$c_2$	-2.339	-0.3104	-2.335
$c_3$	-8.0262	-0.1023	-0.8243
$c_4$	0	0	0.1312
$c_5$	0	0	0.2338

TABLE II. Elastic constants  $\mathcal{K}$  (bulk modulus) and  $\mathcal{G}$  (shear modulus) in units of meV per unit cell.

	MoS <sub>2</sub>	Graphene	MoSe <sub>2</sub>	WSe <sub>2</sub>
$\mathcal{K}$	73546	99265	81194	73745
$\mathcal{G}$	59028	99275	71562	63681

#### IV. MOIRÉ PHONON PROPERTIES

Using our CSC model, we calculate the phonon properties of three different moiré bilayers: Graphene, MoS<sub>2</sub>, and a MoSe<sub>2</sub>-WSe<sub>2</sub> heterostructure. Near the  $\Gamma$  point the lowest-energy modes include two shearing modes (S) and one layer breathing (LB) mode. These represent in-plane and out-of-plane motions, respectively, with each layer moving in the opposite direction.

##### A. Low-energy mode frequencies

The phonon dispersion relations are qualitatively similar for twisted bilayer graphene and TMDCs. Here, we focus on graphene. Figure 5 shows the graphene phonon bands at different twist angles  $\theta$ . As  $\theta$  decreases, the frequency where folded clusters of phonon bands appear also decreases, due to the shrinking of the moiré Brillouin zone area. Atomic relaxation due to interlayer interactions becomes more significant as the twist angle decreases, leading to three qualitatively different regimes characterized by the value of  $\theta$ : A “decoupled” regime (large  $\theta$ ), a “soft” regime (moderate  $\theta$ ), and a “relaxed” regime (small  $\theta$ ). The exact values of  $\theta$  separating these regimes are specific to the material. For graphene they are approximately 4.2° and 0.5°, respectively; for MoS<sub>2</sub> they are 7.6° and 1°; and for MoSe<sub>2</sub>-WSe<sub>2</sub> they are 5.5° and 1.0°. In the decoupled regime [Fig. 5(a)] the relatively large twist angle and small moiré scale means there is little atomic relaxation and the net interlayer coupling is very weak. Here, the S mode is slightly positive at  $\Gamma$  with twofold degeneracy (when the distinction between the two S modes becomes important, we shall refer to the lower-energy curve as S<sub>1</sub> and the higher-energy curve as S<sub>2</sub>), while the LB mode is essentially dispersionless. The zero-frequency modes at  $\Gamma$  are the three translational modes. In the soft regime [Fig. 5(b)],

where atomic relaxation starts to become more noticeable, the S mode begins to exhibit imaginary frequencies at the  $\Gamma$  point (plotted as negative values for continuity in the phonon bands). In the relaxed regime [Fig. 5(d)] the low-energy stacking regions grow in size at the expense of the high-energy stacking regions. Thus, most of the atoms are in local energy minima and are therefore resistant to shearing. As a result, the shearing mode frequency becomes positive again.

Such ultrasoft S modes have been discussed in previous work [48]. In the limit of small angles (large moiré cells) that are truly incommensurate, they are zero modes at  $\Gamma$  that correspond to the invariance of the moiré pattern to a horizontal shift of one layer relative to the other [49,50]. Given the complicated structure of the moiré dynamical matrix, the delicate numerical cancellations necessary to reproduce a (near) zero mode are unlikely to occur in practice. For comparison, in standard phonon calculations the zero modes (acoustic phonons, particularly the translational mode with  $z$  invariance in 2D materials) are corrected by imposing an acoustic sum rule that explicitly enforces translational invariance. As discussed previously, we impose such a rule in the CSC model as well, which is why there are no negative-frequency acoustic phonon bands. In the same spirit, to deal with the ultrasoft shearing modes one could impose a “shearing sum rule” to enforce this additional symmetry of moiré structures. Such a rule, however, is more subtle and involved than the acoustic sum rule, and we leave its imposition to future work. The imaginary frequencies are not a simple consequence of numerical sampling error or relaxation effects, as we demonstrate in Appendix D.

In the soft regime, the LB mode becomes dispersive, as seen in Figs. 5(b) and 5(c), but progressively flattens out again as  $\theta$  approaches the relaxed regime, Fig. 5(d). At 1.1°, the LB mode has a crossing with a cluster of folded bands whose frequency decreases as the Brillouin zone shrinks [Fig. 5(c)], and similarly for  $\theta = 0.4^\circ$  [Fig. 5(d)].

We may examine the frequency dependence on twist angle more thoroughly by focusing on the  $\Gamma$  point. Figure 6 compares the S and LB frequencies for graphene, MoS<sub>2</sub>, and MoSe<sub>2</sub>-WSe<sub>2</sub>. The decoupled, soft, and relaxed regimes are shaded blue, white, and brown, respectively. The soft regime begins when the S mode takes negative frequency values, and ends where the slope of  $\omega$  becomes negative at small  $\theta$ . Aside

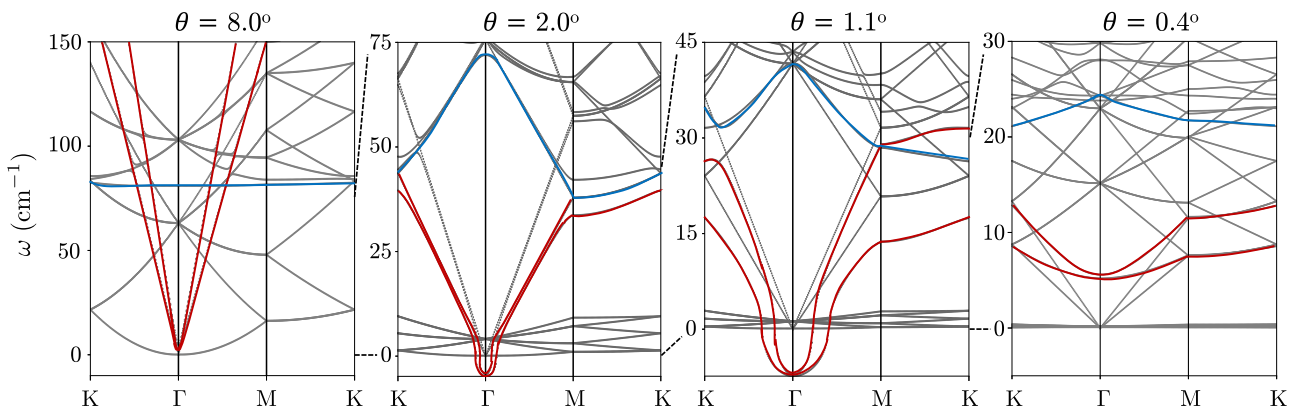


FIG. 5. Phonon bands of graphene as obtained from our CSC model at four representative angles of (a) 8°, (b) 2°, (c) 1.1°, and (d) 0.4°. The two shearing modes are highlighted in red, and the first (lowest energy) LB mode in blue.

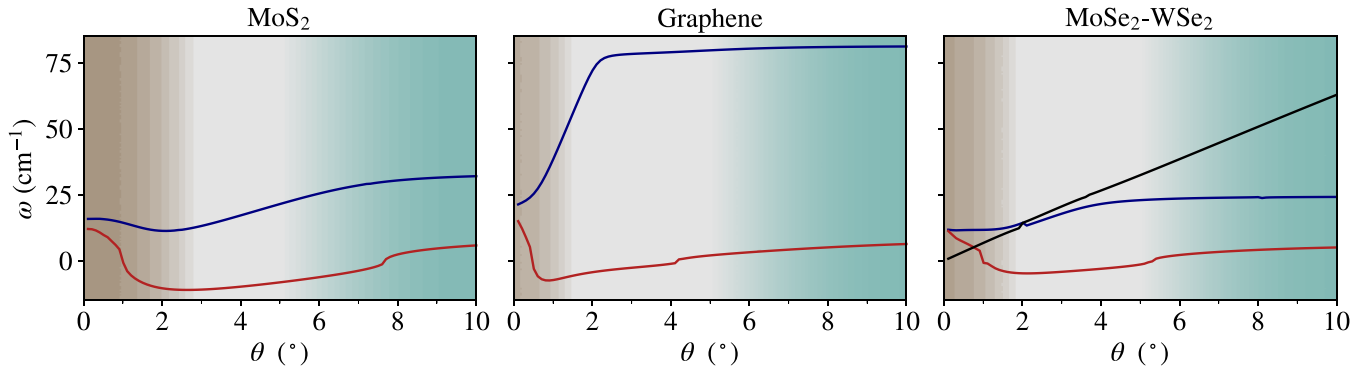


FIG. 6. Frequency of the shearing (red line) and layer breathing (blue line) modes at  $\Gamma$  as a function of twist angle  $\theta$  for various bilayers. The MoSe<sub>2</sub>-WSe<sub>2</sub> heterostructure has an additional LB-like mode that breaks symmetry, labeled SBLB (black line). The background color shades illustrate the transition from the decoupled region (large  $\theta$ , S frequencies positive or nearly 0) in blue shade, to the soft region (from initial dip to negative S frequencies to angle of maximally negative frequency) in white shade, to the relaxed region (upward curve to positive S frequencies) in brown shade.

from the location and width of the soft regime, however, the frequency dependence on  $\theta$  of the S mode is qualitatively similar for all three materials. For MoS<sub>2</sub> and MoSe<sub>2</sub>-WSe<sub>2</sub>, the LB varies smoothly and slowly with  $\theta$ . By contrast, the LB mode in graphene has a comparatively higher frequency in the decoupled regime, which drops sharply near the end of the soft regime. Since the MoSe<sub>2</sub>-WSe<sub>2</sub> heterostructure breaks the layer symmetry, it admits an additional LB-like mode that does not respect the symmetry under layer inversion ( $\mathbf{r} \rightarrow -\mathbf{r}$ ). We refer to this mode as the symmetry-breaking LB (SBLB) mode, and note that it is the only mode that varies linearly in frequency with respect to  $\theta$ .

### B. Real space atomic displacements at the $\Gamma$ point

By performing the inverse Fourier transform of eigenmodes in reciprocal space [Eq. (29)], we obtain the atomic displacement field of each phonon mode in real space. The eigenmodes in reciprocal space are unit vectors, but application of the Fourier transform gives the magnitude of the displacement vectors a physical interpretation. Specifically, the overall magnitudes across various twist angles serve as an indicator for the magnitude of each eigenmode component  $\delta\mathbf{u}(\tilde{\mathbf{G}})$  in reciprocal space. For if most of the magnitude in

reciprocal space is concentrated in the  $\tilde{\mathbf{G}}_0$  component, the real space magnitude will be large, but if most of the magnitude is concentrated in the first shell  $\tilde{\mathbf{G}}_1, \dots, \tilde{\mathbf{G}}_6$ , the phases in the inverse Fourier transform reduce the real space magnitude to a much smaller quantity. In the absence of the moiré interlayer couplings, the magnitude in Fourier space should be concentrated in the  $\tilde{\mathbf{G}}_0$  component, but at smaller values of  $\theta$ , emergence of periodicity of the moiré length scale implies that the magnitude becomes instead concentrated in higher shells. Thus, we should expect the magnitude in real space to fall substantially near the angle at which the magnitudes of the  $\tilde{\mathbf{G}}_0$  component and the  $\tilde{\mathbf{G}}_1, \dots, \tilde{\mathbf{G}}_6$  components intersect.

Figure 7 demonstrates these features in the LB mode by approximating the average real space magnitude through a  $13 \times 13$  mesh discretization of the moiré supercell. For brevity, we have averaged the magnitudes of the six first-shell reciprocal lattice vectors. Note that the magnitude of the  $\tilde{\mathbf{G}}_0$  component can be measured via Raman spectroscopy [35], and thus the real space magnitude across  $\theta$  serves to indicate at which twist angle the mode will be difficult to detect experimentally.

The magnitudes of  $\delta\mathbf{u}(\mathbf{r})$  also allow for comparison of the relative strength between in-plane ( $\delta u_{xy}$ ) and out-of-plane ( $\delta u_z$ ) motion; for example, the S modes satisfy  $\delta u_z \ll \delta u_{xy}$ .

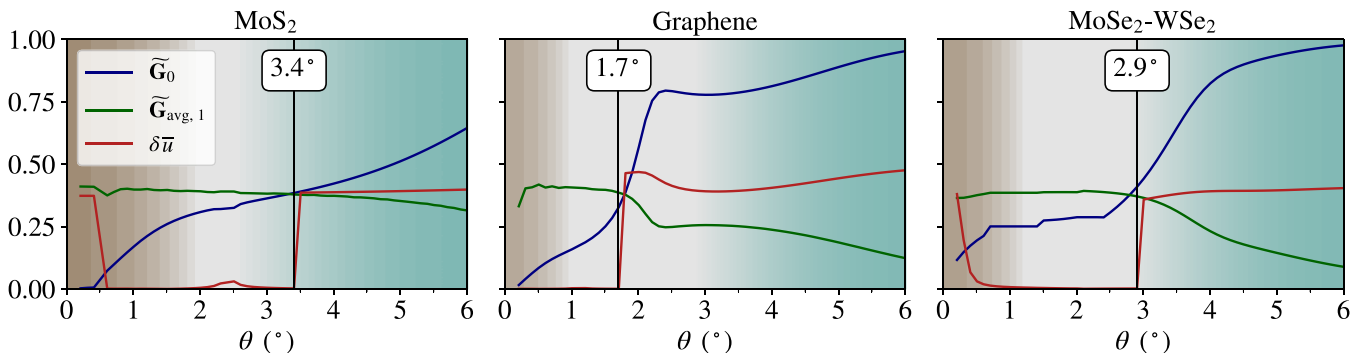


FIG. 7. Average atomic displacement magnitudes in real space ( $\delta\bar{u}$ , red), of the  $\tilde{\mathbf{G}}_0$  component in reciprocal space (blue), and of the average of the first-shell components  $\tilde{\mathbf{G}}_1, \dots, \tilde{\mathbf{G}}_6$  of the LB mode at  $\Gamma$  for MoS<sub>2</sub>, graphene, and MoSe<sub>2</sub>-WSe<sub>2</sub>. The shading of various regimes has the same meaning as in Fig. 6. The vertical black lines indicate the largest value of the twist angle at which  $\delta\bar{u} \rightarrow 0$ .

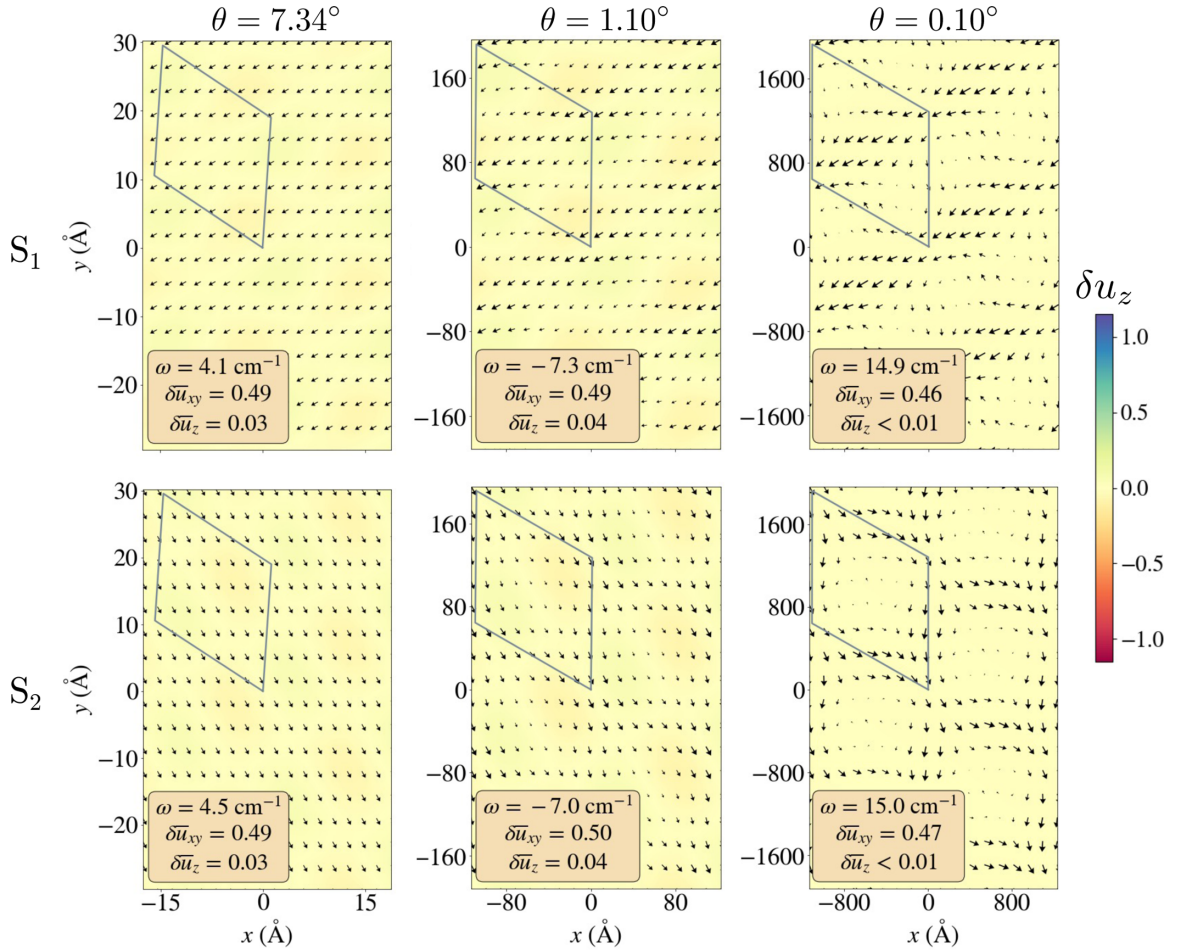


FIG. 8. Real space atomic displacements (in arbitrary units) for the twofold degenerate shearing modes,  $S_1$  and  $S_2$ , of the first layer of graphene at various twist angles. In-plane ( $x, y$ ) displacements are proportional to the arrows and vertical ( $z$ ) displacements are shown in color. The arrows are rescaled for visualization purposes, with the average values of in-plane ( $\delta\bar{u}_{xy}$ ) and out-of-plane ( $\delta\bar{u}_z$ ) magnitudes, rounded to 2 decimal places, shown in the lower insets. The displacements of layer 2 are exactly opposite to those of layer 1. The gray parallelogram outlines a single moiré cell.

This is seen explicitly by visualization of the S and LB atomic displacement fields, from which we may also deduce the geometric structure of the atomic displacements as a function of  $\theta$ . In all figures showing atomic displacement field results from the CSC model, we normalize the magnitudes that correspond to each atomic degree of freedom by the atomic mass  $\sqrt{M_\alpha}$  for each layer, and subsequently average the vectors over the atomic degrees of freedom. We verified numerically that for all modes analyzed in the present work, the vectors for each atomic degree of freedom are identical up to mass normalization, which justifies the averaging. We then renormalize by multiplying the atom-averaged field by  $\sqrt{\sum_\alpha M_\alpha}$ , where  $\alpha$  is the atomic index.

Figure 8 illustrates the evolution of the atomic displacement field of the two S modes,  $S_1$  and  $S_2$ , as a function of  $\theta$ . In all cases, the S mode is dominated by in-plane displacements and is opposite in the two layers. In the decoupled regime ( $7.34^\circ$ ) the displacement is uniform. As  $\theta$  decreases, translational symmetry on the graphene unit cell scale is broken and we observe structure at the moiré scale.

In contrast to the S modes, the geometrical structure of the LB mode remains invariant as  $\theta$  changes. Figure 9 shows the LB modes at two different angles in which the two layers have equal and opposite displacements along the  $z$  direction, similarly to the LB mode in AB bilayer graphene. However, while the LB mode in an untwisted bilayer system corresponds to a negligible in-plane motion, the moiré LB modes correspond to swirling motion around the corners of the moiré supercell in opposing directions between layers, which resembles the relaxation pattern in twisted bilayer graphene [41]. This is because the  $\Gamma$  point LB mode changes the interlayer separation on the moiré scale, which modifies the local interlayer energy. To compensate for such an energy cost, the mode adopts an in-plane rotation that changes the total AA area. Consistent with Fig. 7, the relative magnitude of the LB mode displacement field varies substantially with respect to twist angle, as shown in the insets of Fig. 9.

Finally, we examine the real space structure of SBLB mode in the MoSe<sub>2</sub>-WSe<sub>2</sub> heterostructure. Unlike the LB mode where the in-plane motions are opposite at every real space position, the SBLB mode in the heterostructure breaks layer

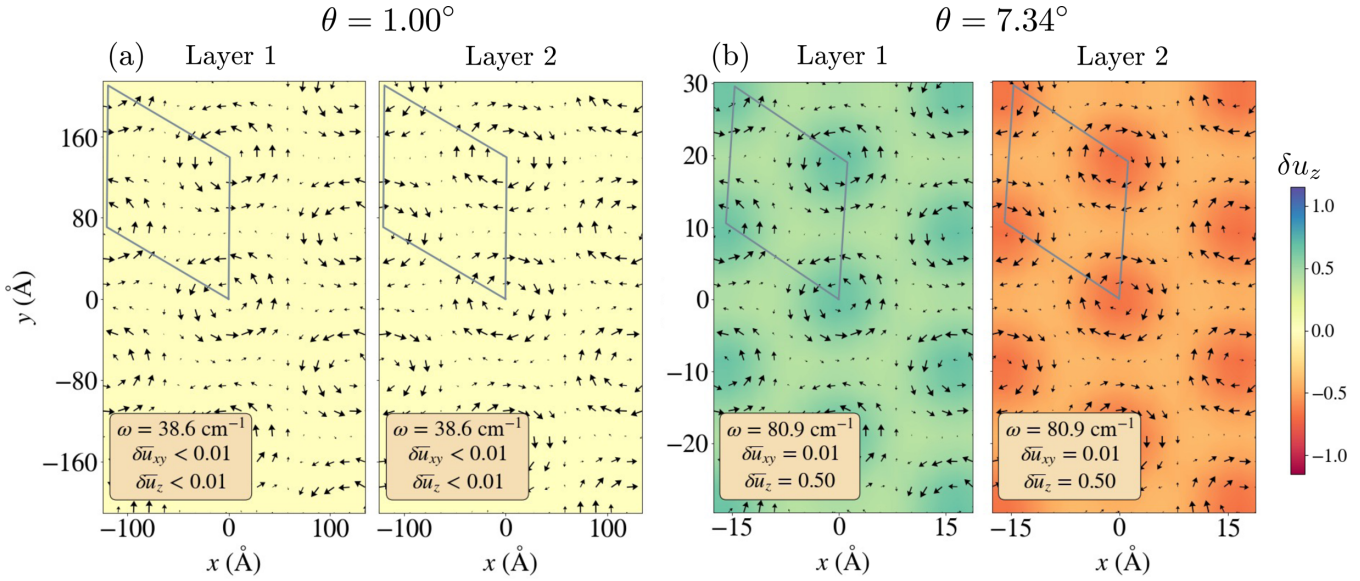


FIG. 9. LB atomic displacements of graphene at twist angles (a)  $1.00^\circ$  and (b)  $7.34^\circ$ . Color scale and insets are the same as in Fig. 8. For each angle, the left (right) panel shows layer 1 (2).

symmetry. As shown in Fig. 10, both layers share the same in-plane rotation direction. Note that there is a preferential in-plane rotation direction in the heterostructure; we did not observe a degenerate SBLB mode with the other rotation direction. The out-of-plane motions are small but opposite between layers.

The atomic displacements in real space may be examined beyond the  $\Gamma$  point, though that is beyond the scope of discussion in this paper. We provide a brief discussion in Appendix E.

### C. Higher energy LB (LB<sub>2</sub> and LB<sub>3</sub>) modes

In addition to the lowest-energy LB mode analyzed above (which we now call LB<sub>1</sub>), we observe two LB modes of higher

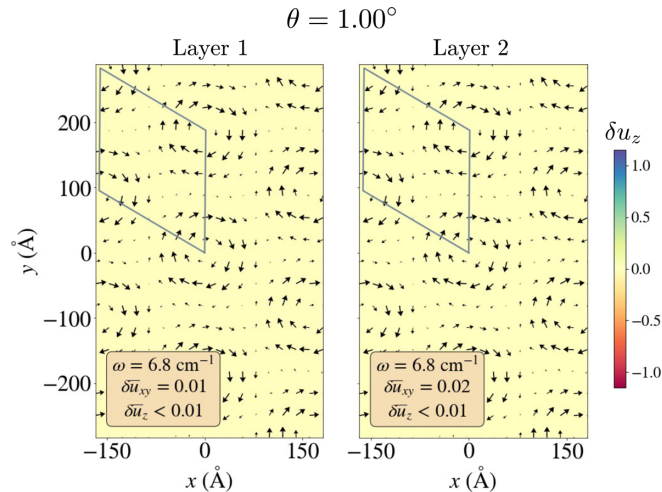


FIG. 10. MoSe<sub>2</sub>-WSe<sub>2</sub> SBLB mode real space atomic displacements at  $\theta = 1.00^\circ$ . The insets and color scale are the same as in Fig. 9.

frequency. The key characteristics of moiré LB modes are the oppositely oriented swirling in-plane motion and the opposite out-of-plane motion between each layer at every point  $\mathbf{r}$ ; these are properties that all three LB modes exhibit. However, in LB<sub>1</sub>, as shown in Fig. 9, the out-of-plane displacement has a uniform direction within each layer. This does not hold for the LB<sub>2</sub> and LB<sub>3</sub> modes for all  $\theta$ . To quantify the uniformity in the out-of-plane displacement direction, we define the following quantity:

$$\mathcal{U}_{\text{LB}}^{12} = \frac{1}{N^2} \sum_{i=1}^{N^2} \delta_{\text{sgn}[\delta u_z^{(1)}(\mathbf{r}_i)], 1} \delta_{\text{sgn}[\delta u_z^{(2)}(\mathbf{r}_i)], -1}, \quad (31)$$

where  $N$  is the sampling grid size in the moiré supercell and  $\delta u_z^{(\ell)}(\mathbf{r}_i)$  is the  $z$  component of the phonon at point  $\mathbf{r}_i$  in layer  $\ell$ . Equation (31) essentially estimates the fraction of area where  $\delta u_z^{(1)}$  points in the positive direction while  $\delta u_z^{(2)}$  points in the negative direction. Since it does not matter which layer breathes in which out-of-plane direction, we define the breathing uniformity value  $\mathcal{U}_{\text{LB}} = \max(\mathcal{U}_{\text{LB}}^{12}, \mathcal{U}_{\text{LB}}^{21})$ , which estimates the fraction of the moiré cell that breathes in the same out-of-plane direction. A translational mode with  $z$  invariance has  $\mathcal{U}_{\text{LB}} = 0$ , and a perfectly uniform breathing motion (such as that of LB<sub>1</sub>) has  $\mathcal{U}_{\text{LB}} = 1$ . A maximally nonuniform breathing motion has  $\mathcal{U}_{\text{LB}} = 0.5$ , which means that at each point, the field is equally likely to point in either direction.

Figure 11 shows the two higher-frequency LB modes for each material, color-coded by  $\mathcal{U}_{\text{LB}}$ . We observe that the uniformity of the breathing motion is dependent of  $\theta$ . In fact, at any value of  $\theta$ , one mode is maximally uniform while the other is not. Hence, we define the LB<sub>2</sub> mode as the maximally uniform mode and the LB<sub>3</sub> mode as the other mode. This identification is not well defined in degenerate transition regions, such as that near  $\theta = 6.0^\circ$  in MoS<sub>2</sub> and  $\theta \lesssim 1.0^\circ$  in all three materials. In MoS<sub>2</sub> only, the LB<sub>2</sub> and LB<sub>3</sub> modes change order in the frequency scale.

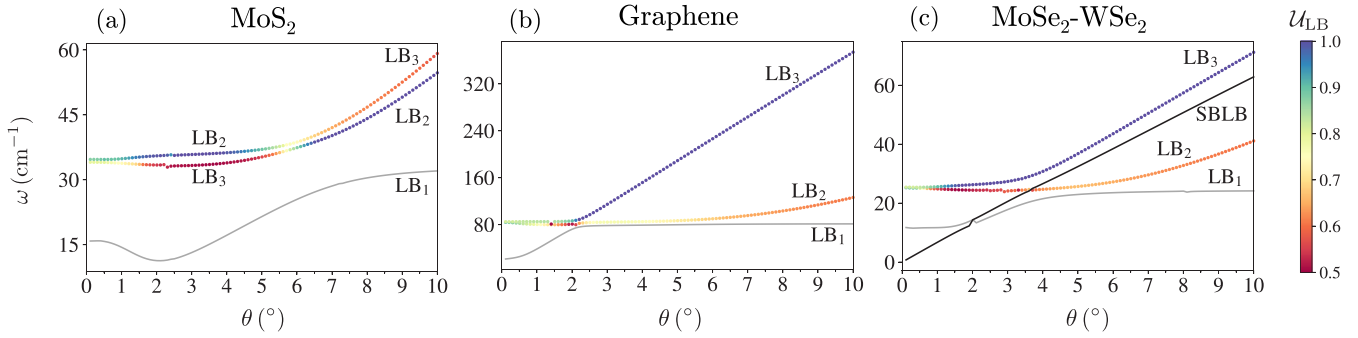


FIG. 11. The frequencies of the LB<sub>2</sub> and LB<sub>3</sub> modes color-coded by their uniformity value  $\mathcal{U}_{LB}$  (common scale on the right) for (a) MoS<sub>2</sub>, (b) graphene, and (c) MoSe<sub>2</sub>-WSe<sub>2</sub>. LB<sub>1</sub> in gray and SBLB in black are shown for comparison.

In Fig. 12, we provide an example of a uniform versus a nonuniform higher-frequency LB mode in MoS<sub>2</sub> at  $\theta = 3.0^\circ$ . The nonuniformity manifests in the difference in direction of out-of-plane motion near the AA regions versus the AB/BA regions.

## V. SUMMARY

We developed an accurate and efficient model for calculating phonon properties in bilayer moiré vdW heterostructures, which is based on the configuration space continuum (CSC) formalism. Within this formalism, we showed that phonons related to moiré patterns in twisted bilayers can be calculated directly from ensembles of phonons related to rigidly

shifted bilayers at various arrangements, with first-principles accuracy.

By analyzing the low-frequency shearing (S) and layer breathing (LB) modes in three representative materials (twisted bilayer graphene, bilayer MoS<sub>2</sub>, and a MoSe<sub>2</sub>-WSe<sub>2</sub> heterostructure), we showed that the physics of moiré-pattern phonons depend on the twist angle  $\theta$ . Phonon frequencies vary slowly and smoothly with  $\theta$ , while the atomic displacement magnitude is more sensitive to small changes in twist angle near certain  $\theta$  values. Our CSC model can be applied more generally to classes of bilayers beyond the three materials on which we focus here, such as bilayers that are oppositely oriented (the pristine bilayer has one layer rotated by 180° relative to the other) or Janus materials.

Despite its efficiency and accuracy, the CSC model is limited in its present form to lowest-frequency modes and negative shearing frequencies due to the approximations inherent in the model. In the work presented here, we only expand the moiré dynamical matrix to the first shell of the moiré Brillouin zone. Increasing the cutoff radius would allow for the extension to higher frequency modes, although a new derivation of the acoustic sum rule is required. Future work to broaden the scope of the CSC model may include introducing  $\mathbf{k}$  dependence on the off-diagonal components of the moiré dynamical matrix in order to remove the low-frequency approximation. Moreover, the CSC model may be applied to further investigate relatively low-energy phonon modes of interest, such as chiral phonons [51–53].

Building upon previous experimental studies with Raman spectroscopy [31–35], the phonon features derived by our CSC model may be used to guide further experimental comparison for other materials. The most direct application of the CSC model is as a phonon framework for a model of electron-phonon coupling in moiré materials. Ultimately, such studies will provide a theoretical foundation for the origin of strongly correlated states in moiré systems, and the extent to which phonons play a role in such phenomena.

## ACKNOWLEDGMENTS

We thank Lukas Linhart, Florian Libisch, and Stephen Carr for their helpful advice. The calculations described in this paper were performed on the FASRC Cannon cluster supported by the FAS Division of Science Research Computing Group at Harvard University, and NERSC, a U.S. Depart-

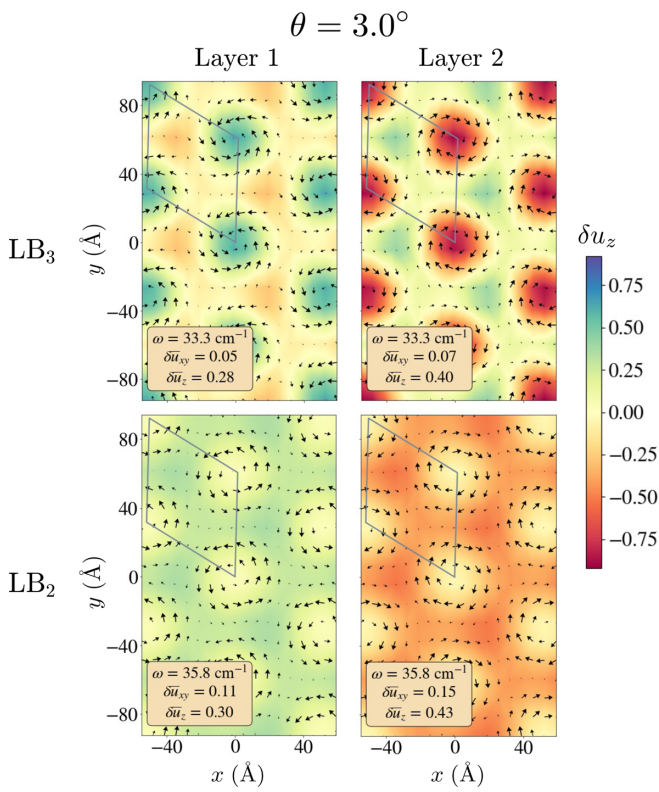


FIG. 12. Atomic displacement fields of LB<sub>2</sub> and LB<sub>3</sub> in MoS<sub>2</sub> at  $\theta = 3.0^\circ$ . The insets and color scale are the same as in Fig. 8.

ment of Energy Office of Science User Facility located at Lawrence Berkeley National Laboratory, operated under Contract No. DE-AC02-05CH11231. J.L. acknowledges funding support from the Harvard Herchel-Smith and PRISE fellowships. Z.Z., D.T.L., and E.K. acknowledge funding from the STC Center for Integrated Quantum Materials, NSF Grant No. DMR-1231319, NSF Award No. DMR-1922172, and the Army Research Office under Cooperative Agreement No. W911NF-21-2-0147. Z.Z. and E.K. also acknowledge funding from the Simons Foundation, Award No. 896626. D.T.L. also acknowledges funding from the U.S. Department of Energy, Office of Science, under Award No. DE-SC0019300. M.A. acknowledges funding from the NSF under Award No. DMR-1922172 and the Army Research Office under Grant No. W911NF-14-1-0247.

#### APPENDIX A: GENERALIZED STACKING FAULT ENERGY

The generalized stacking fault energy (GSFE) functional measures the energy as a function of stacking configuration. We evaluate the GSFE landscape  $V^{\text{GSFE}}(\mathbf{b})$  according to a first shell expansion from Carr *et al.* [41]. Since the Fourier expansion is written in coefficients of  $e^{i\mathbf{G}\cdot\mathbf{b}}$ , with  $\mathbf{G}$  a reciprocal lattice vector of the bilayer at a configuration  $\mathbf{b}$ , denote for a Bravais lattice basis  $\mathbf{a}_1 = a_0(1, 0)$ ,  $\mathbf{a}_2 = a_0(1/2, \sqrt{3}/2)$ :

$$\begin{pmatrix} \mu \\ \nu \end{pmatrix} = \frac{2\pi}{a} \begin{bmatrix} 1 & -1/\sqrt{3} \\ 0 & 2/\sqrt{3} \end{bmatrix} \mathbf{b}. \quad (\text{A1})$$

Using  $120^\circ$  rotational and  $(\mu, \nu) \rightarrow (\nu, \mu)$  symmetries, the GSFE can then be expanded to first shell as

$$\begin{aligned} V^{\text{GSFE}} = & c_0 + c_1[\cos(\mu) + \cos(\nu) + \cos(\mu + \nu)] \\ & + c_2[\cos(\mu + 2\nu) + \cos(\mu - \nu) + \cos(2\mu + \nu)] \\ & + c_3[\cos(2\mu) + \cos(2\nu) + \cos(2\mu + 2\nu)] \\ & + c_4[\sin(\mu) + \sin(\nu) - \sin(\mu + \nu)] \\ & + c_5[\sin(2\mu + 2\nu) - \sin(2\mu) - \sin(2\nu)] \end{aligned} \quad (\text{A2})$$

with  $\mathbf{c} = (c_0, \dots, c_5) \in \mathbb{R}^6$ . We fit  $V^{\text{GSFE}}$  with least-squares linear regression in the above basis. For quantities with inversion reciprocal space symmetry, or equivalently  $V^{\text{GSFE}}(\mu, \nu) = V^{\text{GSFE}}(-\mu, -\nu)$ ,  $c_4 = c_5 = 0$ . The parameters in  $\mathbf{c}$  are important for computing the relaxation in configuration space [41,42]. Figure 13 shows the fits to the GSFE for each of the 3 bilayers we studied. The coefficients we obtain for each material are given in Table I.

#### APPENDIX B: COMPUTATIONAL DETAILS

We study the moiré phonons of graphene,  $\text{MoS}_2$ , and the  $\text{MoSe}_2\text{-WSe}_2$  heterostructure, with lattice constants 2.457, 3.178, 3.306 Å, respectively. Following the implementation in Fig. 1, we sample a  $9 \times 9$  uniform mesh in configuration space. For each configuration, we perform DFT calculations using the Vienna *Ab initio* Simulation Package (VASP) [54–57] with the  $\text{r}^2\text{SCAN-rVV10}$  van der Waals functional [58], an 800 eV plane-wave energy cutoff,  $17 \times 17$   $k$ -point grid, and  $10^{-6}$  eV electronic convergence threshold. The horizontal positions of the carbon atoms (graphene)

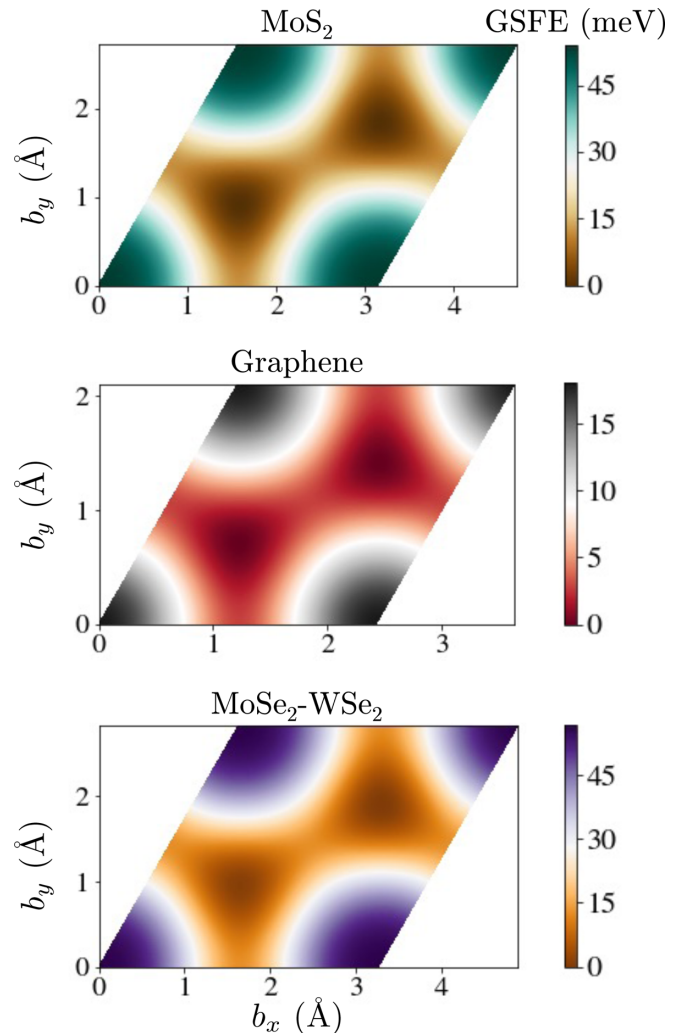


FIG. 13. GSFE of  $\text{MoS}_2$ , graphene, and  $\text{MoSe}_2\text{-WSe}_2$  fitted with first-order Fourier basis regression.

and metal atoms (TMDCs) are held fixed, but the remaining ionic coordinates are allowed to relax until the forces are below  $10^{-6}$  eV/Å. We then compute the interatomic force constants using the frozen phonon approach with a  $3 \times 3$  supercell, converging electronic self-consistent loops to  $10^{-8}$  eV. We repeat the frozen phonon calculations for the monolayers, but use a  $6 \times 6$  supercell for improved accuracy.

We then construct the rigid moiré dynamical matrix in the manner described in Sec. II C of the main text, enforcing pristine monolayer and bilayer symmetries numerically with the phonopy and hiPhive libraries as well as the acoustic sum rule from Sec. II E [59,60]. Finally, continuum relaxation is implemented by the procedure outlined in Sec. II D from Carr *et al.* [41]. Continuum relaxation requires input parameters of the GSFE coefficients from Table I and the monolayer bulk ( $\mathcal{K}$ ) and shear ( $\mathcal{G}$ ) moduli, given in Table II.

Direct DFT calculations of moiré phonons were performed for a commensurate  $7.34^\circ$  graphene supercell containing 244 carbon atoms constructed from a primitive cell with lattice constant  $a = 2.467$  Å. These calculations used VASP and the PBE exchange correlation functional [61] with zero damping DFT-D3 van der Waals corrections [62],  $3 \times 3 \times$

1  $k$ -point sampling, and a plane-wave energy cutoff of 400 eV. The atomic displacements, force constants, and phonon band structure were computed with the phonopy package.

MD calculations of the moiré phonons are performed using the LAMMPS package [63]. Phonons are computed by direct diagonalization of the system's dynamical matrix [28] obtained after relaxing the twisted bilayer's atomic positions [47]. The carbon-carbon intralayer interactions are modeled via the second generation REBO potential [64]. The interlayer interactions are instead modeled via the Kolmogorov-Crespi (KC) potential [65], using the parametrization of Ref. [66]. The starting intralayer carbon-carbon distance is set equal to  $a_0 = 1.3978 \text{ \AA}$ , corresponding to the equilibrium bond length of the adopted REBO potential, giving a lattice parameter of  $a \approx 2.42 \text{ \AA}$ . Geometric optimizations are performed using the FIRE algorithm [67]. The atomic positions are relaxed toward equilibrium until the total forces acting on each atom become less than  $10^{-6} \text{ eV/atom}$ .

### APPENDIX C: EMPIRICAL CONTINUUM MODEL

One approach to obtaining moiré phonons is through an empirical continuum model based on the relaxation model introduced in Carr *et al.* [41]. The approach is introduced by Koshino and Son [29]; we briefly review and adapt it here. To obtain the in-plane phonon modes, we perturb around the equilibrium positions after relaxation. Here, we assume a homobilayer, for which the relaxation in layers 1 and 2 has symmetry  $\mathbf{u}^{(1)}(\mathbf{r}) = -\mathbf{u}^{(2)}(\mathbf{b}) \equiv \mathbf{u}$ . The equilibrium position is calculated by minimizing the total energy, which is the sum of the interlayer energy that is the integral of the GSFE in configuration space [Eq. (A2)],

$$E^{\text{inter}}(\mathbf{u}) = \int V^{\text{GSFE}}(\mathbf{u} + \mathbf{b}) d^2\mathbf{b}, \quad (\text{C1})$$

and the intralayer elastic energy,

$$E^{\text{intra}}(\mathbf{u}) = 2 \int \Phi^{\text{intra}}(\mathbf{u}) d^2\mathbf{b}, \quad (\text{C2})$$

with

$$\Phi^{\text{intra}}(\mathbf{u}) = \frac{1}{2} \nabla_{\mathbf{r}} \mathbf{u}(\mathbf{b}) : C : \nabla_{\mathbf{r}} \mathbf{u}(\mathbf{b}), \quad (\text{C3})$$

where  $\nabla_{\mathbf{r}}$  is the real space gradient and  $C$  is the linear elasticity tensor. For in-plane deformations,  $C$  is a rank-4 tensor with its components defined as follows:

$$\begin{aligned} C_{11ij} &= \begin{pmatrix} \mathcal{K} + \mathcal{G} & 0 \\ 0 & \mathcal{G} \end{pmatrix}, & C_{12ij} &= \begin{pmatrix} 0 & \mathcal{K} - \mathcal{G} \\ \mathcal{G} & 0 \end{pmatrix}, \\ C_{21ij} &= \begin{pmatrix} 0 & \mathcal{G} \\ \mathcal{K} - \mathcal{G} & 0 \end{pmatrix}, & C_{22ij} &= \begin{pmatrix} \mathcal{G} & 0 \\ 0 & \mathcal{K} + \mathcal{G} \end{pmatrix}. \end{aligned} \quad (\text{C4})$$

A lattice vibration perturbs the equilibrium positions, leading to an additional kinetic energy contribution:

$$T = \sum_{\ell=1}^2 \int \frac{\rho}{2} [(\dot{U}_x^{(\ell)})^2 + (\dot{U}_y^{(\ell)})^2] d^2\mathbf{r}, \quad (\text{C5})$$

where  $\rho$  is the area density of a single layer ( $\rho = 7.61 \times 10^{-7} \text{ kg/m}^2$  for graphene),  $\ell$  labels the layer, and  $\dot{U}_{\alpha}^{(\ell)}$  is the time derivative of the cartesian component  $\alpha = x, y$  of  $U$  in layer  $\ell$ .

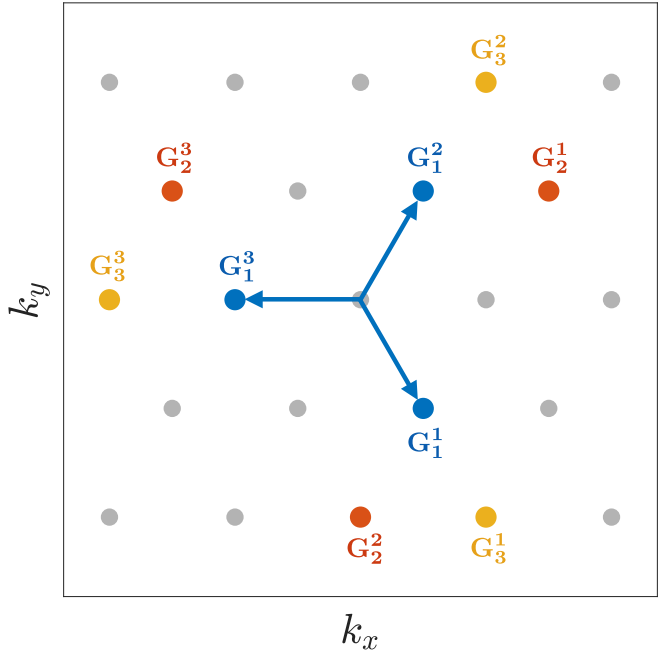


FIG. 14. Definition of reciprocal lattice vectors in Eq. (C6), where the subscript labels different shells (different colors) and the superscript labels different components within the same shell (same color). The gray scatter points are reciprocal lattice vectors.

The Lagrangian of the system is given by  $\mathcal{L} = T - (E^{\text{intra}} + E^{\text{inter}})$  as a function of  $\mathbf{U}^{(\ell)}(\mathbf{r})$ . We define  $\mathbf{U}^{\pm} = \mathbf{U}^{(2)} \pm \mathbf{U}^{(1)}$  and rewrite  $\mathcal{L}$  as a function of  $\mathbf{U}^{\pm}$ . Let us rewrite the GSFE from Eq. (A2) in a more compact form:

$$V^{\text{GSFE}}(\mathbf{b}) = c_0 + \sum_{j=1}^3 \sum_{n=1}^3 c_j \cos (\mathbf{G}_j^n \cdot \mathbf{b}), \quad (\text{C6})$$

where  $\mathbf{G}_j^n$  are the monolayer reciprocal lattice vectors defined in Fig. 14. Here, the subscript  $j$  labels the shell (vectors that are the same distance from the origin) and the superscript  $n$  labels the element within the shell. For simplicity we assume symmetry between AB and BA stacking and only consider the cosine components of the GSFE here ( $c_1, c_2, c_3$ ), but the following results can be easily generalized to include the sine components ( $c_4, c_5, c_6$ ).

The equations of motion for  $\mathbf{U}^-$  are given as follows:

$$\begin{aligned} \frac{1}{2} \rho \ddot{U}_x^- &= \frac{1}{2} \left( \mathcal{K} + \frac{\mathcal{G}}{3} \right) \left( \frac{\partial^2 U_x^-}{\partial x^2} + \frac{\partial^2 U_y^-}{\partial x \partial y} \right) \\ &\quad + \frac{\mathcal{G}}{2} \left( \frac{\partial^2 U_x^-}{\partial x^2} + \frac{\partial^2 U_x^-}{\partial y^2} \right) \\ &\quad + \sum_{j=1}^3 \sum_{n=1}^3 G_{j,x}^n c_j \sin [\mathbf{G}_j^n \cdot (\mathbf{b} + \mathbf{u}^-)], \\ \frac{1}{2} \rho \ddot{U}_y^- &= \frac{1}{2} \left( \mathcal{K} + \frac{\mathcal{G}}{3} \right) \left( \frac{\partial^2 U_y^-}{\partial y^2} + \frac{\partial^2 U_x^-}{\partial x \partial y} \right) \\ &\quad + \frac{\mathcal{G}}{2} \left( \frac{\partial^2 U_y^-}{\partial x^2} + \frac{\partial^2 U_y^-}{\partial y^2} \right) \\ &\quad + \sum_{j=1}^3 \sum_{n=1}^3 G_{j,y}^n c_j \sin [\mathbf{G}_j^n \cdot (\mathbf{b} + \mathbf{u}^-)], \end{aligned} \quad (\text{C7})$$

where  $G_{j,\alpha}^n$  is the  $\alpha = x, y$  component of  $\mathbf{G}_j^n$ . Note that  $\mathbf{U}(\mathbf{r})$  is the real space displacement and  $\mathbf{u}(\mathbf{b})$  is the configuration space displacement and they are related by the linear transformation in Eq. (24). The terms on the second lines of Eq. (C7) that are proportional to  $c_j$  come from the GSFE, which depends only on  $\mathbf{U}^-$ , the difference between relaxation in layer 1 and layer 2, and not on  $\mathbf{U}^+$ . Thus the equations of motion for  $\mathbf{U}^+$  are given by replacing  $\mathbf{U}^-$  with  $\mathbf{U}^+$  and dropping the terms proportional to  $c_j$ . Because  $\mathbf{U}^+$  represents equal motion in both layers, its fluctuations yield the acoustic phonons of a monolayer.

To determine the moiré phonons we study  $\mathbf{U}^-$  and consider a small vibration around the static equilibrium relaxation:

$$\mathbf{U}^-(\mathbf{r}, t) = \mathbf{U}_0^-(\mathbf{r}) + \delta\mathbf{U}^-(\mathbf{r}, t), \quad (C8)$$

where  $\mathbf{U}_0^-$  is the static relaxation that minimizes the total energy,  $E^{\text{intra}} + E^{\text{inter}}$ , and  $\delta\mathbf{U}^-(\mathbf{r}, t)$  is the perturbation around  $\mathbf{U}_0^-$ , which constitutes the phonon modes. We define the following Fourier coefficients to express the displacement and equations of motion in Fourier space:

$$\begin{aligned} \mathbf{U}_0^-(\mathbf{r}) &= \sum_{\tilde{\mathbf{G}}} \mathbf{U}_{0,\tilde{\mathbf{G}}} e^{i\tilde{\mathbf{G}} \cdot \mathbf{r}}, \\ \delta\mathbf{U}^-(\mathbf{r}, t) &= e^{-i\omega t} \sum_{\mathbf{q}} \delta\mathbf{U}_{\mathbf{q}}^- e^{i\mathbf{q} \cdot \mathbf{r}}, \\ \sin [\mathbf{G}_j^n \cdot (\mathbf{b} + \mathbf{u}^-)] &= \sum_{\tilde{\mathbf{G}}} f_{j,\tilde{\mathbf{G}}}^n e^{i\tilde{\mathbf{G}} \cdot \mathbf{r}}, \\ \cos [\mathbf{G}_j^n \cdot (\mathbf{b} + \mathbf{u}^-)] &= \sum_{\tilde{\mathbf{G}}} h_{j,\tilde{\mathbf{G}}}^n e^{i\tilde{\mathbf{G}} \cdot \mathbf{r}}, \end{aligned} \quad (C9)$$

where  $\tilde{\mathbf{G}}$  is the moiré reciprocal lattice vector. Note that  $\tilde{\mathbf{G}} \cdot \mathbf{r} = \mathbf{G} \cdot \mathbf{b}$ , where  $\mathbf{G}$  is the monolayer reciprocal lattice vector. We expand Eq. (C7) around the static solution  $\mathbf{U}_0$  to the first order in  $\delta\mathbf{U}$  and perform a Fourier expansion to obtain the equation of motion for the perturbation part:

$$\rho\omega^2 \delta\mathbf{U}_{\tilde{\mathbf{G}}+\mathbf{q}}^- = \hat{K}_{\tilde{\mathbf{G}}+\mathbf{q}} \delta\mathbf{U}_{\tilde{\mathbf{G}}+\mathbf{q}}^- - 4 \sum_{\tilde{\mathbf{G}}'} \hat{V}_{\tilde{\mathbf{G}}-\tilde{\mathbf{G}}'} \delta\mathbf{U}_{\tilde{\mathbf{G}}'+\mathbf{q}}^-, \quad (C10)$$

where

$$\hat{K}_{\tilde{\mathbf{G}}} = \begin{pmatrix} (\mathcal{K} + \frac{4}{3}\mathcal{G})G_x^2 + \mathcal{G}G_y^2 & (\mathcal{K} + \frac{\mathcal{G}}{3})G_x G_y \\ (\mathcal{K} + \frac{\mathcal{G}}{3})G_x G_y & (\mathcal{K} + \frac{4}{3}\mathcal{G})G_y^2 + \mathcal{G}G_x^2 \end{pmatrix} \quad (C11)$$

and

$$\hat{V}_{\tilde{\mathbf{G}}} = \sum_{j=1}^3 c_j \sum_{n=1}^3 h_{j,\tilde{\mathbf{G}}}^n \begin{pmatrix} G_{j,x}^n G_{j,x}^n & G_{j,x}^n G_{j,y}^n \\ G_{j,x}^n G_{j,y}^n & G_{j,y}^n G_{j,y}^n \end{pmatrix}. \quad (C12)$$

Here, the  $\hat{V}_{\tilde{\mathbf{G}}-\tilde{\mathbf{G}}'}$  is essentially an interlayer scattering selection rule that couples  $\tilde{\mathbf{G}}$  and  $\tilde{\mathbf{G}}'$ . After obtaining the equilibrium relaxation displacement vectors  $\mathbf{U}_0^-$  self-consistently [41], we solve the eigenvalue problem in Eq. (C10) to obtain the eigenmodes  $\omega^2$ .

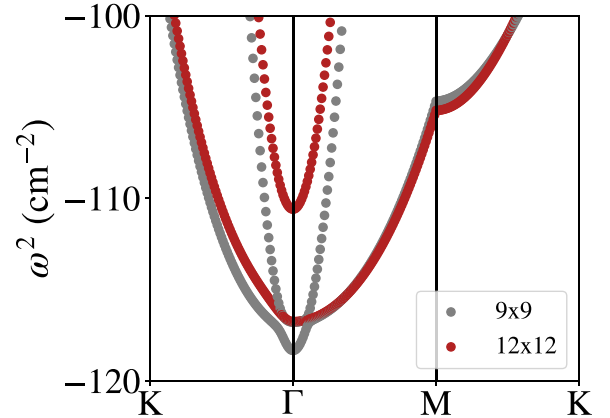


FIG. 15. Eigenvalues  $\omega^2$  of the dynamical matrix of MoS<sub>2</sub> at 2.0° for two configuration space sampling densities, 9 × 9 and 12 × 12.

#### APPENDIX D: FURTHER DISCUSSION OF THE SOFT REGIME

A natural question from the analysis of the CSC model is whether the imaginary shearing frequencies in the soft regime are simply due to sampling issues. In this section we provide evidence that this is not the case.

Our calculations in the continuum approach have used a 9 × 9 discretization of configuration space. Thus, one might imagine the possibility that this discretization was not sufficiently dense to cover enough configurations, and caused numerical error that led to soft modes. However, as Fig. 15 illustrates for bilayer MoS<sub>2</sub> with a representative twist angle of  $\theta = 2.0^\circ$ , an improved sampling grid of 12 × 12 does not significantly increase the negative eigenvalues; in fact, if we were to plot the values of  $\omega$ , that is, the square root of the results shown in Fig. 15, the difference is visually indistinguishable.

Moreover, as mentioned earlier, relaxation cannot alone fix the softness of the shearing modes. For a twist angle of 2.0° the relaxation produces only very small changes to the configuration vectors  $\mathbf{b}$ , as shown in Fig. 16. Hence, the problem of ultrasoft shearing modes in the soft regime is a

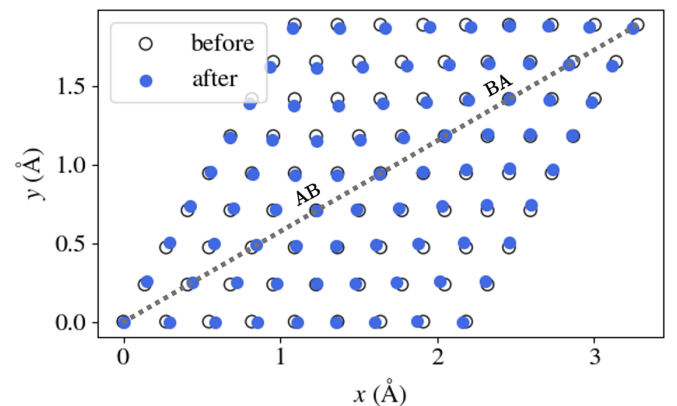


FIG. 16. Updated configurations of MoS<sub>2</sub> at  $\theta = 2.0^\circ$  after continuum relaxation.

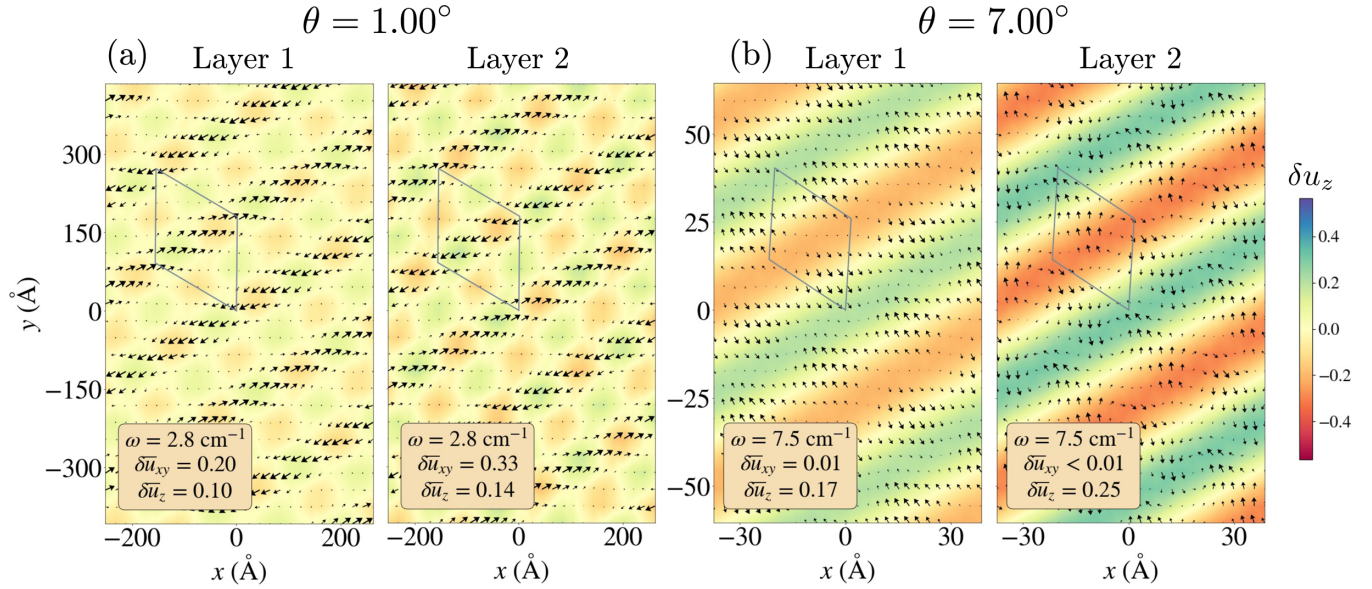


FIG. 17. Displacement fields of the first folded band in MoS<sub>2</sub> at  $M$ . For each of (a) and (b), the left (right) side displays layer 1 (2). The periodicity is of a  $2 \times 2$  moiré supercell.

problem more subtle than that of sampling or relaxation in configuration space.

#### APPENDIX E: REAL SPACE DISPLACEMENT AT OTHER HIGH-SYMMETRY POINTS

The real space analysis in this paper has focused on the low-energy modes at  $\Gamma$ . However, the CSC model permits analysis of fields at any  $k$  point, computed in the same way but with an extra phase given by the  $k$  point to the inverse Fourier transform. Every field at  $\Gamma$  has the period of one moiré

cell  $\lambda$ . However, at  $M$ , some (but not all) bands have the period of 2 moiré lengths, while at  $K$  some have the period of 3 moiré lengths. This is to be expected, as for a Bravais hexagonal lattice with basis vectors oriented  $120^\circ$  apart,  $M = \frac{1}{2}\tilde{g}_1 + \frac{1}{2}\tilde{g}_2$  and  $K = \frac{2}{3}\tilde{g}_1 + \frac{1}{3}\tilde{g}_2$ , where  $\{\tilde{g}_i\}$  is the reciprocal lattice basis. Examples of these periodicities are shown respectively in Figs. 17 and 18 on MoS<sub>2</sub> on the first folded band, which is the lowest-energy band at each  $k$  point stemming from the first folded cluster. For example, the analogous band for graphene is the cluster between the S and LB modes of Fig. 5(a).

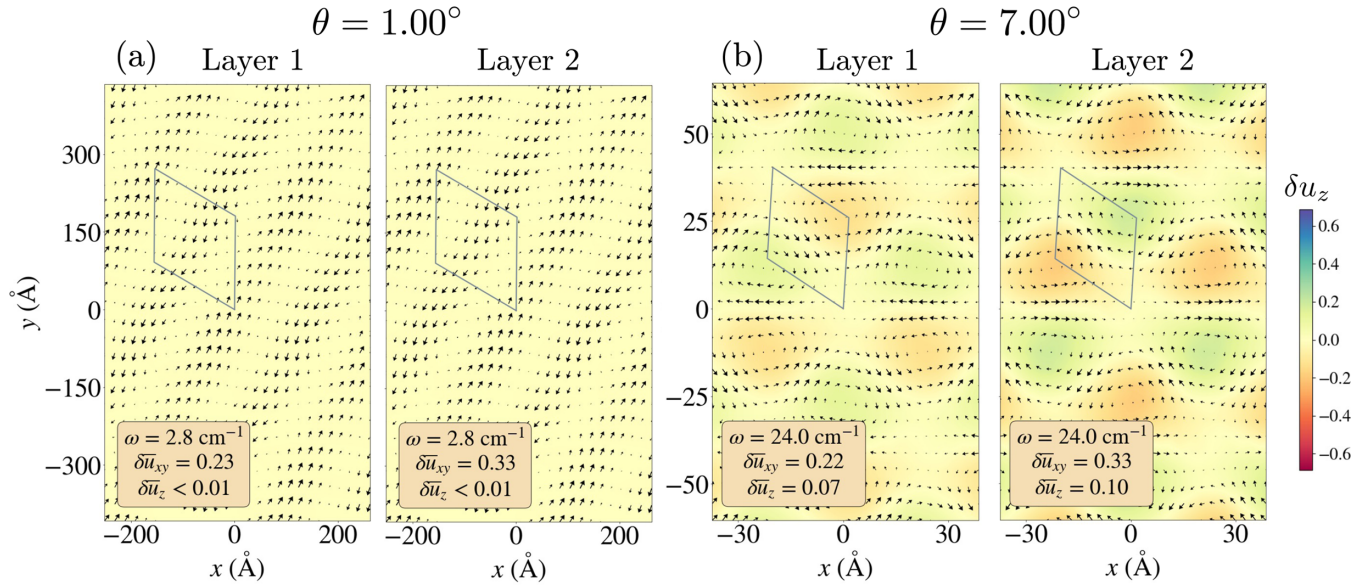


FIG. 18. Displacement fields of the first folded band in MoS<sub>2</sub> at  $K$ . For each of (a) and (b), the left (right) side displays layer 1 (2). The maximum periodicity is of a  $3 \times 3$  moiré supercell.

[1] S. Carr, D. Massatt, S. Fang, P. Cazeaux, M. Luskin, and E. Kaxiras, Twistrronics: Manipulating the electronic properties of two-dimensional layered structures through their twist angle, *Phys. Rev. B* **95**, 075420 (2017).

[2] M. Yankowitz, J. Jung, E. Laksono, N. Leconte, B. L. Chittari, K. Watanabe, T. Taniguchi, S. Adam, D. Graf, and C. R. Dean, Dynamic band-structure tuning of graphene moiré superlattices with pressure, *Nature (London)* **557**, 404 (2018).

[3] X. Liu, Z. Hao, E. Khalaf, J. Y. Lee, Y. Ronen, H. Yoo, D. Haei Najafabadi, K. Watanabe, T. Taniguchi, A. Vishwanath, and P. Kim, Tunable spin-polarized correlated states in twisted double bilayer graphene, *Nature (London)* **583**, 221 (2020).

[4] Z. Song, Z. Wang, W. Shi, G. Li, C. Fang, and B. A. Bernevig, All Magic Angles in Twisted Bilayer Graphene are Topological, *Phys. Rev. Lett.* **123**, 036401 (2019).

[5] G. W. Burg, J. Zhu, T. Taniguchi, K. Watanabe, A. H. MacDonald, and E. Tutuc, Correlated Insulating States in Twisted Double Bilayer Graphene, *Phys. Rev. Lett.* **123**, 197702 (2019).

[6] Y. Cao, D. Rodan-Legrain, O. Rubies-Bigorda, J. M. Park, K. Watanabe, T. Taniguchi, and P. Jarillo-Herrero, Tunable correlated states and spin-polarized phases in twisted bilayer-bilayer graphene, *Nature (London)* **583**, 215 (2020).

[7] S. Moriyama, Y. Morita, K. Komatsu, K. Endo, T. Iwasaki, S. Nakahara, Y. Noguchi, Y. Wakayama, E. Watanabe, D. Tsuya, K. Watanabe, and T. Taniguchi, Observation of superconductivity in bilayer graphene/hexagonal boron nitride superlattices, *arXiv:1901.09356*.

[8] Y. Cao, V. Fatemi, S. Fang, K. Watanabe, T. Taniguchi, E. Kaxiras, and P. Jarillo-Herrero, Unconventional superconductivity in magic-angle graphene superlattices, *Nature (London)* **556**, 43 (2018).

[9] Y. Cao, V. Fatemi, A. Demir, S. Fang, S. L. Tomarken, J. Y. Luo, J. D. Sanchez-Yamagishi, K. Watanabe, T. Taniguchi, E. Kaxiras, R. C. Ashoori, and P. Jarillo-Herrero, Correlated insulator behaviour at half-filling in magic-angle graphene superlattices, *Nature (London)* **556**, 80 (2018).

[10] X. Lu, P. Stepanov, W. Yang, M. Xie, M. A. Aamir, I. Das, C. Urgell, K. Watanabe, T. Taniguchi, G. Zhang, A. Bachtold, A. H. MacDonald, and D. K. Efetov, Superconductors, orbital magnets and correlated states in magic-angle bilayer graphene, *Nature (London)* **574**, 653 (2019).

[11] M. Xie and A. H. MacDonald, Nature of the Correlated Insulator States in Twisted Bilayer Graphene, *Phys. Rev. Lett.* **124**, 097601 (2020).

[12] L. Wang, E.-M. Shih, A. Ghiotto, L. Xian, D. A. Rhodes, C. Tan, M. Claassen, D. M. Kennes, Y. Bai, B. Kim, K. Watanabe, T. Taniguchi, X. Zhu, J. Hone, A. Rubio, A. Pasupathy, and C. R. Dean, Correlated electronic phases in twisted bilayer transition metal dichalcogenides, *Nat. Mater.* **19**, 861 (2020).

[13] F. Li, W. Wei, H. Wang, B. Huang, Y. Dai, and T. Jacob, Intrinsic electric field-induced properties in Janus MoSSe van der Waals structures, *J. Phys. Chem. Lett.* **10**, 559 (2019).

[14] F. Wu, T. Lovorn, E. Tutuc, and A. H. MacDonald, Hubbard Model Physics in Transition Metal Dichalcogenide Moiré Bands, *Phys. Rev. Lett.* **121**, 026402 (2018).

[15] K. Liu, L. Zhang, T. Cao, C. Jin, D. Qiu, Q. Zhou, A. Zettl, P. Yang, S. G. Louie, and F. Wang, Evolution of interlayer coupling in twisted molybdenum disulfide bilayers, *Nat. Commun.* **5**, 4966 (2014).

[16] F. Wu, T. Lovorn, E. Tutuc, I. Martin, and A. H. MacDonald, Topological Insulators in Twisted Transition Metal Dichalcogenide Homobilayers, *Phys. Rev. Lett.* **122**, 086402 (2019).

[17] K. Zhang, Y. Guo, D. T. Larson, Z. Zhu, S. Fang, E. Kaxiras, J. Kong, and S. Huang, Spectroscopic signatures of interlayer coupling in janus MoSSe/MoS<sub>2</sub> heterostructures, *ACS Nano* **15**, 14394 (2021).

[18] K. Tran, G. Moody, F. Wu, X. Lu, J. Choi, K. Kim, A. Rai, D. A. Sanchez, J. Quan, A. Singh, J. Embley, A. Zepeda, M. Campbell, T. Autry, T. Taniguchi, K. Watanabe, N. Lu, S. K. Banerjee, K. L. Silverman, S. Kim *et al.*, Evidence for moiré excitons in van der Waals heterostructures, *Nature (London)* **567**, 71 (2019).

[19] C. Jin, E. C. Regan, A. Yan, M. Iqbal Bakti Utama, D. Wang, S. Zhao, Y. Qin, S. Yang, Z. Zheng, S. Shi, K. Watanabe, T. Taniguchi, S. Tongay, A. Zettl, and F. Wang, Observation of moiré excitons in WSe<sub>2</sub>/WS<sub>2</sub> heterostructure superlattices, *Nature (London)* **567**, 76 (2019).

[20] E. M. Alexeev, D. A. Ruiz-Tijerina, M. Danovich, M. J. Hamer, D. J. Terry, P. K. Nayak, S. Ahn, S. Pak, J. Lee, J. I. Sohn, M. R. Molas, M. Koperski, K. Watanabe, T. Taniguchi, K. S. Novoselov, R. V. Gorbachev, H. S. Shin, V. I. Fal'ko, and A. I. Tartakovskii, Resonantly hybridized excitons in moiré superlattices in van der Waals heterostructures, *Nature (London)* **567**, 81 (2019).

[21] K. L. Seyler, P. Rivera, H. Yu, N. P. Wilson, E. L. Ray, D. G. Mandrus, J. Yan, W. Yao, and X. Xu, Signatures of moiré-trapped valley excitons in MoSe<sub>2</sub>/WSe<sub>2</sub> heterobilayers, *Nature (London)* **567**, 66 (2019).

[22] P. Rivera, J. R. Schaibley, A. M. Jones, J. S. Ross, S. Wu, G. Aivazian, P. Klement, K. Seyler, G. Clark, N. J. Ghimire, J. Yan, D. G. Mandrus, W. Yao, and X. Xu, Observation of long-lived interlayer excitons in monolayer MoSe<sub>2</sub>-WSe<sub>2</sub> heterostructures, *Nat. Commun.* **6**, 6242 (2015).

[23] A. M. van der Zande, J. Kunstmänn, A. Chernikov, D. A. Chenet, Y. You, X. Zhang, P. Y. Huang, T. C. Berkelbach, L. Wang, F. Zhang, M. S. Hybertsen, D. A. Muller, D. R. Reichman, T. F. Heinz, and J. C. Hone, Tailoring the electronic structure in bilayer molybdenum disulfide via interlayer twist, *Nano Lett.* **14**, 3869 (2014).

[24] M. Angeli and A. H. MacDonald,  $\Gamma$  valley transition metal dichalcogenide moiré bands, *Proc. Natl. Acad. Sci. USA* **118**, e2021826118 (2021).

[25] F. Wu, A. H. MacDonald, and I. Martin, Theory of Phonon-Mediated Superconductivity in Twisted Bilayer Graphene, *Phys. Rev. Lett.* **121**, 257001 (2018).

[26] B. Lian, Z. Wang, and B. A. Bernevig, Twisted Bilayer Graphene: A Phonon-Driven Superconductor, *Phys. Rev. Lett.* **122**, 257002 (2019).

[27] T. Cea and F. Guinea, Coulomb interaction, phonons, and superconductivity in twisted bilayer graphene, *Proc. Natl. Acad. Sci. USA* **118**, e2107874118 (2021).

[28] M. Angeli, E. Tosatti, and M. Fabrizio, Valley Jahn-Teller Effect in Twisted Bilayer Graphene, *Phys. Rev. X* **9**, 041010 (2019).

[29] M. Koshino and Y.-W. Son, Moiré phonons in twisted bilayer graphene, *Phys. Rev. B* **100**, 075416 (2019).

[30] A. C. Gadelha, D. A. A. Ohlberg, C. Rabelo, E. G. S. Neto, T. L. Vasconcelos, J. L. Campos, J. S. Lemos, V. Ornelas, D. Miranda, R. Nadas, F. C. Santana, K. Watanabe, T. Taniguchi, B. van Troeye, M. Lamparski, V. Meunier, V.-H. Nguyen, D. Paszko, J.-C. Charlier, L. C. Campos *et al.*, Localization of lattice dynamics in low-angle twisted bilayer graphene, *Nature (London)* **590**, 405 (2021).

[31] J. Campos-Delgado, L. G. Cançado, C. A. Achete, A. Jorio, and J.-P. Raskin, Raman scattering study of the phonon dispersion in twisted bilayer graphene, *Nano Res.* **6**, 269 (2013).

[32] J.-B. Wu, X. Zhang, M. Ijäs, W.-P. Han, X.-F. Qiao, X.-L. Li, D.-S. Jiang, A. C. Ferrari, and P.-H. Tan, Resonant Raman spectroscopy of twisted multilayer graphene, *Nat. Commun.* **5**, 5309 (2014).

[33] S. Huang, L. Liang, X. Ling, A. A. Puretzky, D. B. Geohegan, B. G. Sumpter, J. Kong, V. Meunier, and M. S. Dresselhaus, Low-frequency interlayer raman modes to probe interface of twisted bilayer MoS<sub>2</sub>, *Nano Lett.* **16**, 1435 (2016).

[34] M.-L. Lin, Q.-H. Tan, J.-B. Wu, X.-S. Chen, J.-H. Wang, Y.-H. Pan, X. Zhang, X. Cong, J. Zhang, W. Ji, P.-A. Hu, K.-H. Liu, and P.-H. Tan, Moiré phonons in twisted bilayer MoS<sub>2</sub>, *ACS Nano* **12**, 8770 (2018).

[35] J. Quan, L. Linhart, M.-L. Lin, D. Lee, J. Zhu, C.-Y. Wang, W.-T. Hsu, J. Choi, J. Embley, C. Young, T. Taniguchi, K. Watanabe, C.-K. Shih, K. Lai, A. H. MacDonald, P.-H. Tan, F. Libisch, and X. Li, Phonon renormalization in reconstructed MoS<sub>2</sub> moiré superlattices, *Nat. Mater.* **20**, 1100 (2021).

[36] S. Dai, Y. Xiang, and D. J. Srolovitz, Twisted bilayer graphene: Moiré with a twist, *Nano Lett.* **16**, 5923 (2016).

[37] N. N. T. Nam and M. Koshino, Lattice relaxation and energy band modulation in twisted bilayer graphene, *Phys. Rev. B* **96**, 075311 (2017).

[38] M. I. Español, D. Golovaty, and J. P. Wilber, Discrete-to-continuum modeling of weakly interacting incommensurate chains, *Phys. Rev. E* **96**, 033003 (2017).

[39] M. I. Español, D. Golovaty, and J. P. Wilber, Discrete-to-continuum modelling of weakly interacting incommensurate two-dimensional lattices, *Proc. R. Soc. London, Ser. A* **474**, 20170612 (2018).

[40] N. Leconte, S. Javvaji, J. An, A. Samudrala, and J. Jung, Relaxation effects in twisted bilayer graphene: A multiscale approach, *Phys. Rev. B* **106**, 115410 (2022).

[41] S. Carr, D. Massatt, S. B. Torrisi, P. Cazeaux, M. Luskin, and E. Kaxiras, Relaxation and domain formation in incommensurate two-dimensional heterostructures, *Phys. Rev. B* **98**, 224102 (2018).

[42] Z. Zhu, P. Cazeaux, M. Luskin, and E. Kaxiras, Modeling mechanical relaxation in incommensurate trilayer van der Waals heterostructures, *Phys. Rev. B* **101**, 224107 (2020).

[43] D. Massatt, M. Luskin, and C. Ortner, Electronic density of states for incommensurate layers, [arXiv:1608.01968](https://arxiv.org/abs/1608.01968).

[44] P. Cazeaux, M. Luskin, and E. B. Tadmor, Analysis of rippling in incommensurate one-dimensional coupled chains, [arXiv:1606.02619](https://arxiv.org/abs/1606.02619).

[45] E. Cancès, P. Cazeaux, and M. Luskin, Generalized Kubo formulas for the transport properties of incommensurate 2D atomic heterostructures, *J. Math. Phys.* **58**, 063502 (2017).

[46] P. Cazeaux, M. Luskin, and D. Massatt, Energy minimization of two dimensional incommensurate heterostructures, *Arch. Ration. Mech. Anal.* **235**, 1289 (2020).

[47] M. Angeli, D. Mandelli, A. Valli, A. Amaricci, M. Capone, E. Tosatti, and M. Fabrizio, Emergent  $D_6$  symmetry in fully relaxed magic-angle twisted bilayer graphene, *Phys. Rev. B* **98**, 235137 (2018).

[48] I. Maity, M. H. Naik, P. K. Maiti, H. R. Krishnamurthy, and M. Jain, Phonons in twisted transition-metal dichalcogenide bilayers: Ultrasoft phasons and a transition from a superlubric to a pinned phase, *Phys. Rev. Res.* **2**, 013335 (2020).

[49] R. Bistritzer and A. H. MacDonald, Moiré bands in twisted double-layer graphene, *Proc. Natl. Acad. Sci. USA* **108**, 12233 (2011).

[50] H. Ochoa, Moiré-pattern fluctuations and electron-phason coupling in twisted bilayer graphene, *Phys. Rev. B* **100**, 155426 (2019).

[51] L. Zhang and Q. Niu, Chiral Phonons at High-Symmetry Points in Monolayer Hexagonal Lattices, *Phys. Rev. Lett.* **115**, 115502 (2015).

[52] N. Suri, C. Wang, Y. Zhang, and D. Xiao, Chiral phonons in moiré superlattices, *Nano Lett.* **21**, 10026 (2021).

[53] I. Maity, A. A. Mostofi, and J. Lischner, Chiral valley phonons and flat phonon bands in moiré materials, *Phys. Rev. B* **105**, L041408 (2022).

[54] G. Kresse and J. Hafner, *Ab initio* molecular dynamics for liquid metals, *Phys. Rev. B* **47**, 558 (1993).

[55] G. Kresse and J. Hafner, *Ab initio* molecular-dynamics simulation of the liquid-metal–amorphous–semiconductor transition in germanium, *Phys. Rev. B* **49**, 14251 (1994).

[56] G. Kresse and J. Furthmüller, Efficiency of *ab-initio* total energy calculations for metals and semiconductors using a plane-wave basis set, *Comput. Mater. Sci.* **6**, 15 (1996).

[57] G. Kresse and J. Furthmüller, Efficient iterative schemes for *ab initio* total-energy calculations using a plane-wave basis set, *Phys. Rev. B* **54**, 11169 (1996).

[58] J. W. Furness, A. D. Kaplan, J. Ning, J. P. Perdew, and J. Sun, Accurate and numerically efficient r<sup>2</sup>SCAN meta-generalized gradient approximation, *J. Phys. Chem. Lett.* **11**, 8208 (2020).

[59] A. Togo and I. Tanaka, First principles phonon calculations in materials science, [arXiv:1506.08498](https://arxiv.org/abs/1506.08498).

[60] F. Eriksson, E. Fransson, and P. Erhart, The Hiphive package for the extraction of high-order force constants by machine learning, *Adv. Theory Simul.* **2**, 1800184 (2019).

[61] J. P. Perdew, K. Burke, and M. Ernzerhof, Generalized Gradient Approximation Made Simple, *Phys. Rev. Lett.* **77**, 3865 (1996).

[62] S. Grimme, J. Antony, S. Ehrlich, and H. Krieg, A consistent and accurate *ab initio* parametrization of density functional dispersion correction (DFT-D) for the 94 elements H–Pu, *J. Chem. Phys.* **132**, 154104 (2010).

[63] A. P. Thompson, H. M. Aktulga, R. Berger, D. S. Bolintineanu, W. M. Brown, P. S. Crozier, P. J. in't Veld, A. Kohlmeyer, S. G. Moore, T. D. Nguyen, R. Shan, M. J. Stevens, J. Tranchida, C. Trott, and S. J. Plimpton, LAMMPS—a flexible simulation tool for particle-based materials modeling at the atomic, meso, and continuum scales, *Comput. Phys. Commun.* **271**, 108171 (2022).

[64] D. W. Brenner, O. A. Shenderova, J. A. Harrison, S. J. Stuart, B. Ni, and S. B. Sinnott, A second-generation reactive empirical bond order (REBO) potential energy expression for hydrocarbons, *J. Phys.: Condens. Matter* **14**, 783 (2002).

[65] A. N. Kolmogorov and V. H. Crespi, Registry-dependent interlayer potential for graphitic systems, *Phys. Rev. B* **71**, 235415 (2005).

[66] W. Ouyang, D. Mandelli, M. Urbakh, and O. Hod, Nanoserpents: Graphene nanoribbon motion on two-dimensional hexagonal materials, *Nano Lett.* **18**, 6009 (2018).

[67] E. Bitzek, P. Koskinen, F. Gähler, M. Moseler, and P. Gumbsch, Structural Relaxation Made Simple, *Phys. Rev. Lett.* **97**, 170201 (2006).